Journal of Alloys and Compounds 1039 (2025) 183050

Contents lists available at ScienceDirect

Journal of Alloys and Compounds

journal homepage: www.elsevier.com/locate/jalcom

Deposition of High-Entropy Alloy (HEA) coatings by HVOF and cold gas spray

Giovanni Bolelli [a,*], Maria Francesca Bonilauri [a], Luca Bortolotti [a], Alessia Bruera [a], Lorenzo Ferrari [a], Magdalena Lassinantti Gualtieri [a], Luca Lusvarghi [a], Stefania Morelli [a], Felice Palladino [a], Alessandro Togni [a], Alvise Bianchin [b], Enrico Forlin [b], Giulia Gigante [c], Edoardo Rossi [c], Marco Sebastiani [c], Genís Clavé [d], Camila Barreneche [d], Sergi Dosta [d,*]

[a] Department of Engineering "Enzo Ferrari", University of Modena and Reggio Emilia, Via Pietro Vivarelli 10/1, Modena, MO 41125, Italy
[b] MBN Nanomaterialia s.r.l., Via Giacomo Bortolan, 42, Carbonera, TV 31050, Italy
[c] Department of Civil, Computer Science and Aeronautical Technologies Engineering, Roma Tre University, Via Vito Volterra, 62, Rome 00146, Italy
[d] Department of Materials Science and Physical Chemistry, University of Barcelona, Martí i Franquès, 1-11, Barcelona 08028, Spain

ARTICLE INFO

Keywords:
High-Entropy Alloys
High Velocity Oxygen-Fuel (HVOF)
Cold Gas Spraying (CGS)
Sliding Wear
Electrochemical Polarization
Nanoindentation

ABSTRACT

High-entropy alloy (HEA) coatings were deposited by high-velocity oxygen fuel (HVOF) and cold gas spraying (CGS) using mechanically alloyed feedstock materials, as an alternative to conventional coatings such as Stellite. Cr-Mn-Fe-Co-Ni and $Al_x(Cr_{20}Mn_{25}Fe_{40}Ni_{15})_{100-x}$ (x = 0, 10, 14) alloys were considered. Due to the high reactivity of the mechanically alloyed feedstock, the HVOF-sprayed HEAs contained 20 – 40 vol% oxide inclusions, with greater oxidation in the Al-free compositions. Conversely, CGS coatings retained the microstructure of the feedstock powders, which contained finely dispersed oxides from the mechanical alloying process. Nanoindentation mapping revealed that both the FCC and BCC phases in the coatings were much harder than those in bulk HEAs, because of the small grain size and finely dispersed oxides. On the macroscale, the brittle oxide inclusions in the HVOF coatings resulted in a lower hardness and indentation modulus than those of the CGS coatings. However, oxide inclusions were beneficial to sliding wear resistance because they limited the size of the metal areas that could be sheared off. In fact, the metallic phases suffered adhesive wear because they did not exhibit strengthening mechanisms such as stress-induced phase changes. The sliding wear rates of the coatings were therefore higher than those of HVOF-sprayed Stellite, which undergoes stress-induced martensitic transformation. In electrochemical polarization tests, most of the HVOF HEA coatings had lower corrosion current densities than HVOF-sprayed Stellite, despite narrower passivity ranges that were further worsened by adding Al. The CGS coatings had poor corrosion resistance because their plastically deformed microstructure increased their reactivity.

1. Introduction

High-entropy alloys (HEAs) have gained increasing attention in recent years because of the vast unexplored potential of the central region of multicomponent phase diagrams [1–5]. These alloys consist of mixtures (in identical or similar amounts) of 5 or 6 elements, and frequently develop simple solid solutions with high symmetry. This is often attributed to one of their four "core effects", namely entropy stabilization: elements randomly distributed in a lattice - with several equivalent sites due to symmetry - generate many equivalent configurations, i.e., high entropy [6–8]. This is believed to prevail over the enthalpy gain often associated with the formation of intermetallics and ordered structures.

In fact, entropy stabilization might be overly simplistic for the sometimes complex behaviour of multi-elements [6,7]. It is not always as effective as it is sometimes claimed to be, and in any case, entropy-driven stabilization decreases with decreasing temperature. For example, not only does element segregation often occur during slow cooling of HEA castings, but long-term annealing can give rise to second phases, such as σ- or Laves phases. The formation of the latter might not be observed under standard processing conditions for kinetic reasons, i.e. diffusion to form equilibrium phases might be too slow to take place at

* Corresponding authors.
E-mail addresses: giovanni.bolelli@unimore.it (G. Bolelli), sdosta@ub.edu (S. Dosta).

https://doi.org/10.1016/j.jallcom.2025.183050
Received 14 June 2025; Received in revised form 11 August 2025; Accepted 13 August 2025
Available online 14 August 2025

low temperatures.

Systems that form single-phase solid solutions need to respect the classical Hume-Rothery rules [1,7,9–12]. Five families of HEAs have been identified: transition metal-based HEAs with face-centred cubic (FCC) lattices; transition and refractory metal-based HEAs with body-centred cubic (BCC) lattices; light-element HEAs; precious metal-based HEAs, and refractory metal-based HEAs with hexagonal close-packed (HCP) lattices [13]. Even this classification might not always be completely accurate from a thermodynamic point of view: the phase observed at room temperature might also be influenced by kinetic considerations. For example, a recent experimental study [14] showed that, in the equiatomic Cr-Mn-Fe-Co-Ni system, usually regarded as a prototype FCC HEA, an HCP lattice is actually more thermodynamically stable at room temperature. The FCC phase is stable at high temperatures and is therefore the first phase that develops from the melt, e.g. during casting and cladding. However, the FCC-to-HCP transformation that should thermodynamically occur during cooling is so sluggish that it is kinetically hindered under ordinary processing conditions.

In any case, in each of the HEA families listed above, introducing elements with substantial differences in atomic radius, electronegativity, and/or valence electron concentration (VEC) promotes the formation of multi-phase structures and intermetallics. A typical example is the addition of elements such as Al or Ti to FCC-based mixtures of first-period transition metals such as Cr, Mn, Fe, Co, Ni, and/or Cu, which results in a BCC phase.

Sometimes, retaining the multi-element mixture concept but scaling back to simpler, 3- or 4-element systems, known as medium-entropy alloys (MEAs), may yield better properties (e.g., higher mechanical strength) than the parent HEA. This was reviewed by Kwesi Nutor et al. for ternary CoNiFe, CoNiMn, and CoNiV alloys derived as sub-systems of the "classical" CrMnFeCoNi ("Cantor") HEA [15]. Coury et al. also reported on the particularly interesting mechanical properties of CoCrNi ternary systems [16].

The main properties of HEAs and MEAs are attributable to their "core effects", which, in addition to the above-mentioned entropy stabilization effect [13,16–19], include:

- The lattice distortion effect, which provides solid-solution strengthening
- The sluggish diffusion effect, which, although recently criticized for some HEA compositions [16,20], results in limited atomic mobility in the highly distorted lattice. This should result e.g. in extended high-temperature stability as the alloy should be more resistant e.g. against the formation of excessively large second-phase precipitates
- The "cocktail" effect, i.e. synergistic and often unexpected, non-linear effects arising from the multi-element combination.

These alloys thus often exhibit features such as a unique balance of mechanical strength and ductility/toughness [21], or enhanced corrosion resistance [22–24] and tribological responses [25] in comparison with conventional alloys (e.g. steels and stainless steels, ordinary superalloys). Most of these features can be further optimized by tailoring the composition. From a metallurgical point of view, it is possible to control the strengthening mechanisms and promote specific phenomena such as twinning-induced and transformation-induced plasticity (TWIP, TRIP) [3,4,16]. From a tribological perspective, grain refinement and second-phase formation can be exploited to increase the wear resistance [25,26]. The stability of passivation films can be enhanced by the co-existence of multiple elements [27], which results in significant differences in comparison with the composition and properties of passivation films developed by conventional alloys. For example, while Cr-containing HEAs develop Cr-rich passivation films, which is also common in conventional alloys such as stainless steels, the passivation films on HEAs may also contain some unoxidized metallic elements, which reportedly improve compliance with surface stresses [28].

Due to these potentially advantageous features, HEAs are being explored for various practical applications, either as bulk materials, including bulk parts fabricated by additive manufacturing technologies [17,29,30], or as protective coatings. In terms of the latter, many of the studies have focused on laser-cladded HEA layers, as reviewed e.g. in [31–35]. Laser cladding provides specific advantages, such as a metallurgical bonding to the substrate and obtaining fully dense layers free of interconnected pores. Accordingly, the above-mentioned reviews highlight the promising corrosion resistance of laser-cladded HEA coatings. For instance, the corrosion current densities obtained from electrochemical polarization tests in a 3.5 % NaCl aqueous solution are usually $< 1\ \mu A/cm^2$ [36].

Thermal spraying is another commonly used group of deposition techniques. Thermal spray coatings do not develop an equally strong metallurgical bonding to the substrate and often contain some porosity, oxide inclusions, and interlamellar interfaces [37,38]. On the other hand, the lack of a melt pool means that there is no heat-affected zone in the substrate, no risk of coating dilution with the substrate material, and fewer risks of through-thickness solidification cracks as found in laser-cladded layers deposited under non-optimised conditions [36–40]. Each of these families thus has important and specific application fields.

HEA coatings could be used to replace conventional protective materials that exhibit specific criticalities, despite their excellent performance in terms of, e.g. wear or corrosion protection. For example, Stellite alloys, i.e. Co-Cr-W-C systems, are one of the go-to materials when the operating conditions are especially harsh. They have a high resistance to sliding and galling, excellent corrosion resistance [41,42], and can be used as a bulk or coating, with deposition techniques such as cladding or thermal spraying [43–48]. In a previous work we also showed that high-velocity oxygen fuel (HVOF) and cold gas sprayed Stellite-6 coatings possess good sliding wear resistance over a wide range of temperatures and corrosion resistance in water solutions containing chlorine [43,49,50].

Cobalt, however, is hazardous to human health [51–53] and has been classified as carcinogenic in the European Union directive on the Classification, Labelling and Packaging (CLP) of substances [54,55]. Yet cobalt is also a strategic element because of its many important applications (including in cathodes of Li-ion batteries) [56,57]. Cobalt also poses significant sustainability issues associated with its sourcing [5] and therefore its use needs to be reduced or abandoned entirely.

The aim of the present work is thus to explore different HEA compositions containing lower levels or no cobalt for thermal spray coatings as alternatives to conventional coatings such as Stellite-6 against sliding wear and electrochemical corrosion in water environments.

We specifically focus on two thermal spray techniques: HVOF and cold gas spraying (CGS). As a solid-state deposition technique, CGS has the potential to minimize the oxidation issues previously mentioned. However, it can be problematic with BCC-structured powders, which, because of their higher hardness, possess lower solid-state deformability [58]. On the other hand, by relying on both the melting and acceleration of the powder particles, HVOF is not as sensitive to the mechanical properties of the powder, however it is more prone to causing oxidation. Overall, both methods can provide good quality HEA coatings, albeit with different microstructures, as reported e.g. by Silvello et al. [59].

2. Materials and methods

2.1. HEA compositions

Based on the literature, two types of HEA systems were selected in this work.

– The equiatomic Cr-Mn-Fe-Co-Ni (hereafter referred to as the "Cantor") alloy, which is a well-known HEA with a single-phase FCC structure [1] that has already been investigated by other authors as a thermal spray coating and can thus serve as a good reference point. It

still contains substantial amounts of cobalt, although less than in Stellite alloys, where cobalt is the single main constituent.
- The $Al_x(Cr_{20}Mn_{25}Fe_{40}Ni_{15})_{100-x}$ system studied in [60], which is free from Co and whose phase composition and mechanical properties can be adjusted through the Al content. We specifically chose three compositions: x = 0, 10, and 14. The former is an FCC system with lower hardness and higher ductility. The other Al-containing compositions should form a two-phase system with a disordered BCC solid solution along with an ordered BCC intermetallic, which is characterized by higher hardness and lower ductility. These compositions are (1) free of cobalt; (2) rich in Fe, which should reduce their cost; and (3) enable the effect of varying the phase composition to be studied through the addition of Al. These materials are hereafter referred to as Al_0(CrMnFeNi), Al_{10}(CrMnFeNi), and Al_{14}(CrMnFeNi) for x = 0, 10, and 14, respectively.

2.2. Feedstock manufacturing and characterization

All feedstock powders were obtained by mechanical alloying (MA), a well-known and accepted method of producing HEAs [13]. MA was carried out via a proprietary high-energy ball milling (HEBM) process from elemental powders. The MA powders were then classified using sieves and cyclones into two distinct size distributions: −45 + 10 μm, which is suitable for HVOF spraying, and −38 + 10 μm for CGS.

After preliminary experiments, the Cantor powder for CGS needed to be annealed to be deposited. The CGS-grade Cantor powder was therefore annealed at 600 °C for 3 h in an argon atmosphere (VF800 Furnace, Pro.Ba. Srl). This temperature reduced the degree of work-hardening of the powder, i.e. reduced the micro-hardness measured on the cross-section of the powder particles. On the other hand, the Al_x(CrMnFeNi) powders could not be annealed, because preliminary trials showed that annealing at a sufficient temperature to induce recovery of the work-hardened microstructure also led to the formation of large amounts of σ-phase. This then increased the hardness of the particles and impaired their solid-state deformability.

The particle size distributions of all the feedstock materials were verified by laser scattering (Mastersizer 2000, Malvern Panalytical Ltd., Malvern, UK) using ultrasonication in a wet dispersion cell (Hydro-2000).

The phase composition of the powders was assessed by X-ray diffraction (XRD: X'Pert PRO and Empyrean, Malvern Panalytical B.V., Almelo, NL) using Cu-Kα radiation. The patterns were acquired in the $20° < 2\theta < 85°$ range.

The cross-sectional microstructure and chemical composition of the powders were studied by scanning electron microscopy (SEM: Nova NanoSEM 450, FEI – Thermo Fisher Scientific, Eindhoven, NL) and energy-dispersive X-ray (EDX) spectroscopy (Quantax-200 microanalysis system with XFlash6|10 detector, Bruker Nano GmbH, Berlin, Germany). The powders were mixed with a two-component epoxy resin. The resulting mixture was then cured at room temperature. The samples were ground with SiC papers (from P400 to P4000) and sequentially polished using a polycrystalline diamond suspension (3 μm average size) on a woven cloth and a colloidal silica suspension on a non-woven cloth. Because the powders themselves imparted electrical conductivity to the resin, no surface metallization was employed. Quantitative chemical analyses were carried out acquiring three EDX spectra on areas imaged at 400 ×, operating at a 15 kV electron beam acceleration voltage with a live time of 60 s. Carbon and oxygen were excluded from the quantification, since they were also contained in the resin surrounding the particles. The amount of carbon was instead quantified by the oxygen combustion method (TCH600, LECO Corporation, St. Joseph, MI, USA), whilst oxygen, together with nitrogen, were quantified by the inert gas fusion technique (CS230, LECO Corporation). Details can be found in [61]. The EDX results for all other elements were then renormalized to 100 by including the C, O, and N contents thus measured.

2.3. Coating deposition

The HVOF depositions were carried out on AISI304 stainless steel plates sized 60 × 25 × 3 mm, grit-blasted using brown alumina with a median 300 μm particle size (d_{50}) with a handheld blasting equipment operated at a pressure of 5.5 bar. A roughness of Sa ≈ 7 μm was obtained. The plates were then cleaned in an ultrasonic bath with acetone to remove loose grit residuals and contaminations, dried with compressed air, and stored in a stove at 60 °C to prevent humidity build-up prior to deposition.

The deposition was carried out using a Diamond Jet 2600 HVOF system (Oerlikon Metco, Westbury, NY, USA) equipped with a DJ8W torch and a pressurized gravimetric 9MPE-DJ powder feeder.

The torch was mounted on an X-Y translation system and moved back and forth across a rotating mandrel, onto which the plates were loaded. In all cases, the rotation speed of the mandrel and the horizontal traverse speed of the torch were set to achieve a relative torch-to-substrate velocity of 750 mm/s and a pitch distance of 5 mm. Three consecutive passes of the torch were made per deposition cycle. A total of 13 cycles were performed, with a 20 s pause between cycles to allow for substrate cooling. Fixed compressed air jets were directed at the plates to control deposition temperature and prevent the accumulation of overspray between passes.

Prior to deposition, one 3-pass cycle was performed without powder feed and without air cooling to pre-heat the substrates. The powder feeder was then turned on and deposition started as soon as the feed rate stabilized to within ±4 g/min of the desired value, which usually took around or slightly less than 1 min.

During deposition, the surface temperature of the system was monitored with an infrared pyrometer (OPTRIS CTLaser, Luchsinger srl, Curno, Italy), which was pointed to a position away from the torch scan track to prevent artefacts resulting from the emission of the spray jet.

For all powders, three depositions were carried out using three different parameter sets, which were designated as "Run 1" to "Run 3" and included increasingly high flow rates of H_2 and O_2 as detailed in Table 1, while all other parameters were held constant.

In addition, a commercially available Stellite-6 powder (Amperit 344.088, Höganäs, Laufenburg, Germany – nominal particle size distribution −53 +20 μm) was also deposited with the parameters listed in Table 1. The resulting coatings were used as a benchmark.

The CGS depositions were carried out on AISI316 stainless steel 50 × 20 × 5 mm plates, grit-blasted with white corundum (24 mesh) at 6 bar pressure to obtain a roughness of Ra ≈ 4 μm, cleaned with compressed air and again stored in a stove at 60 °C. A PCS100 high-pressure cold-spray system (Plasma Giken, Yorii, Japan) was used, with N_2 as the process gas.

Different depositions were carried out by changing the gas stagnation pressure and the length of the expansion nozzle, while the gas

Table 1
HVOF deposition parameters for all powders.

Parameter setting	Run 1	Run 2	Run 3	Stellite-6
O_2 pressure (psi / MPa)	170 / 1.20			
O_2 flow rate (SLPM)	201	214	228	214
H_2 pressure (psi / MPa)	140 / 0.98			
H_2 flow rate (SLPM)	574	635	656	635
Air pressure (psi / MPa)	100 / 0.7			
Air flow rate (SLPM)	274			313
Stoichiometric ratio	0.9	0.86	0.87	0.88
Powder feed rate (g/min)	20			60
Standoff distance (mm)	250			
Torch-substrate speed (mm/s)	750			
Pitch distance (mm)	5			6
N° of passes per cycle	3			
N° of deposition cycles	13			9
N° of pre-heating cycles	1			
Pause between cycles (s)	20			

stagnation temperature, after some preliminary tests, was maintained at its maximum value (Table 2).

The CGS depositions were performed only with the Al_0(CrMnFeNi) and the (annealed) Cantor powder, whereas the Al_{10}(CrMnFeNi) and Al_{14}(CrMnFeNi) compositions proved impossible to deposit with this technique. In fact, as explained in Section 2.2, none of the Al_x(CrMnFeNi) were amenable to annealing. The precipitation of a tetragonal σ-phase overcame the effects of recrystallizing the work-hardened microstructure of the as-milled power, which resulted in an eventual increase, rather than a decrease, in hardness. While the Al_0(CrMnFeNi) powder was sufficiently soft to be deposited by CGS in as-milled conditions, the as-milled Al_{10}(CrMnFeNi) and Al_{14}(CrMnFeNi) compositions only yielded thin and very defective layers, with substantial erosion during spraying.

2.4. Characterisation of coatings

2.4.1. Microstructure and phase composition

The cross-sectional microstructure and phase composition of the coatings, along with the powders, were analysed by SEM+EDX and XRD, respectively. For XRD analysis, the coating surfaces were ground using SiC-based papers (from P320 to P4000) and polished with polycrystalline diamond (3 μm average size). To prepare cross-sections for SEM+EDX analyses, the coated plates were cut with a metallographic saw and, unlike the powder, were mounted in a phenol resin using a hot-mounting press. The grinding and polishing of the mounted sections were the same as described in Section 2.2. Some of the cross-sectional samples were also analysed by Electron BackScatter Diffraction (EBSD: Bruker QC-200 I with e-Flash1000 detector, Bruker Nano GmbH). After the polishing procedure described above, the samples were also subjected to vibropolishing with a 60 nm colloidal silica suspension to ensure that any plastically deformed layer left by the previous grinding steps had been completely removed.

The quantitative chemical composition of the coatings was measured by acquiring three EDX spectra on the entire coating area visible in images at 400 × magnification, operating under the same conditions as for the powder. Carbon was excluded from the normalization, while oxygen was included because the acquisition area did not cover the resin.

Porosity was measured by image analysis on 8 micrographs in backscattered electron mode at 3000 × , using the ImageJ software (NIH, Bethesda, USA). Thickness was also measured by image analysis on 400 × micrographs.

2.4.2. Micromechanical testing

2.4.2.1. Microhardness. Cross-sections prepared as described in Section 2.4.1 were also employed to measure the microhardness of the coatings by Vickers micro-indentation (Micro-Combi Tester, Anton Paar Tritec, Corcelles, CH) under an applied load of 3 N, with a loading and unloading time of 30 s each and a 15 s hold at maximum load. Twenty indentations were performed on each sample and the hardness was obtained by measuring the length of the indentation diagonals with an optical microscope at 500 × magnification. The results were expressed as mean ± standard deviation.

Table 2
CGS deposition parameters.

Parameter setting	**Run 1**	**Run 2**	**Run 3**
Process gas (N_2) temperature (°C)	1100		
Process gas (N_2) pressure (MPa)	6	7	7
Nozzle type	Glass short	Glass short	Glass long
Standoff distance (mm)	20		
Pitch distance (mm)	1		
N° of passes	3		

2.4.2.2. Spherical nanoindentation. Multi-cycle spherical nanoindentations were made on the same polished cross-sections using an NHT^3 indenter (Anton Paar Tritec) equipped with a spherical diamond indenter with a tip radius of 20 μm. The indentation protocol involved 25 loading / partial unloading cycles, with a quadratic increment of the peak load from 30 mN to 400 mN, unloading to 20 % of each peak load, 10 s loading and unloading time in each cycle, 15 s hold at each maximum load, and 1 s pause between cycles. At least 20 multi-cycle indentations were performed on each sample.

The data were analysed to extract the indentation hardness (H_{IT}) and the indentation modulus (E_{IT}) of each cycle, as well as the complete stress-strain curves in the plastic deformation regime, following the approach employed in [62,63].

The plane-strain indentation modulus (E^*) was computed as:

$$E^* = \quad S/(2a_{eff})$$

where:

S = unloading slope, obtained by fitting the unloading portion of each cycle with a power-law and taking the first derivative at the beginning of unloading, according to the usual Oliver-Pharr analysis method [64].

a_{eff} = effective contact radius at the maximum load of each cycle $= \sqrt{2 \bullet R \bullet h_C - h_C^2}$

R = indenter radius

h_C = contact depth at the maximum load of each cycle, obtained via the Oliver—Pharr method [64].

The indentation hardness (H_{IT}) was defined as the average contact pressure:

$$H_{IT} = F_{\max}/\left(\pi a_{eff}^2\right)$$

where:

$F_{\max}$ = maximum load at each cycle

The stress—strain curves were obtained by assuming that, at each peak load, the characteristic stress was $\sigma = H_{IT}/2.8$ and the characteristic plastic strain was $\varepsilon = 0.2a_{eff}/R$.

In a spherical indentation experiment, the sample only starts to plasticize for sufficiently high loads. The E^* and H_{IT} values obtained before the complete plasticization of the contact are unreliable, because all analysis models rely on the assumption of full plasticization during loading. Therefore, all the data points at contact depths below the level at which the slope of the E^* versus h_C trend was $< 0.5°$ were discarded. In fact, E^* should be independent of the contact depth when the condition for the applicability of the above equations is met, i.e. full plasticization of the contact region during loading.

To identify the true value of the indenter radius R at each contact depth h_C, accounting for deviations from the nominally ideal spherical geometry, the following approach was employed. First, the profile of the indenter was verified by optical profilometry in structured illumination mode (Confosurf profilometer, Confovis GmbH, Jena, Germany, installed on a Nikon Eclipse LV150N optical microscope operated with a 50 × objective). By fitting the overall profile to a spherical shape, the radius was verified as 20 μm, however the profile was not completely spherical next to the tip due to fabrication imperfections. A calibration was therefore performed against a fused silica standard, performing multicycle indentations and reversing the indentation modulus relation to obtain a_{eff} as a function of the h_C value at each cycle. The data were fitted to a polynomial relation.

When analysing the indentation data from the test samples, R was obtained from the fitting curves for h_C values within the contact depth range for the calibration. For $h_C > 4$ μm the radius was assumed to coincide with the nominal value of 20 μm. For intermediate h_C values, R was computed as a linear interpolation between 20 μm and the value at

the maximum h_C attained in the calibration.

2.4.2.3. High speed nanoindentation. High-speed nanoindentation mapping [65] was performed on the polished cross-section, across the thickness of the coatings, to map mechanical properties and local heterogeneity distributions. With a fast test execution speed (from 1 to 5 s for a load-unload cycle), this method, which is based on the standard Oliver-Pharr procedure [33], enables an indentation matrix to be performed over a wide material area, and the large amount of data acquired enables robust statistical analysis to identify the distinct mechanical phases existing in the coatings. A G200 nanoindenter (KLA Corporation, Oak Ridge, TN, USA) with a standard Berkovich tip was used to perform the tests. The same high-speed methodology was employed to calibrate the machine compliance and the indenter area function.

Table 3 shows information on the parameters used to carry out the load-controlled high-speed nanoindentation mapping. The target load was selected from the load-displacement response obtained through preliminary continuous stiffness measurement tests performed on each sample. The lateral extension and number of indents per sample were adjusted based on the time-resolution trade-off. Indent spacing followed the criterion of 10 times the indentation depth, which prevented plastic zones from overlapping, as recommended in [66,67].

After the experiments, the hardness values from the nanoindentation maps were analysed using the Gaussian mixture model (GMM) algorithm, which assumes a normal distribution of the components. This allows for deconvolution of the dataset via an expectation-maximization protocol.

2.4.3. Wear testing

Ball-on-disc sliding wear tests were performed in unidirectional rotation mode according to ASTM G99, using the same polished surfaces described in Section 2.4.1. The counterparts were 3 mm diameter Al_2O_3 balls, with an applied load of 5 N over a sliding distance of 1000 m at a relative sliding speed of 0.4 m/s with a track radius of 7 mm. At least two tests were performed on each sample.

The friction coefficient was measured during the test using a load cell. The volumetric wear loss of the ball was assessed by measuring the diameter of the circular wear scar with an optical microscope (Olympus GS30) after the test and calculating the corresponding volume of the worn-out spherical cap. The volumetric wear loss of the coatings was measured by a structured illumination microscopy technique (Confosurf profilometer, Confovis GmbH, Jena, Germany, mounted on a Nikon Eclipse LV150N optical microscope), operating with a 10 × objective. Wear loss values were then converted to specific wear rates defined as $K = V/(F_N \bullet L)$, where V = volumetric wear loss, F_N = normal force, L = total sliding distance.

The surfaces and cross-sections of the worn samples were examined by SEM + EDX using the same equipment and procedures described in Section 2.4.1. However, in this case, worn surfaces were examined under an inclination angle of 45° to enhance the morphological contrast, while the cross-sections were hot mounted in a transparent acrylic resin to facilitate identification of the wear track.

Additional observations on the cross-section of the worn samples were carried out by transmission electron microscopy (TEM: Talos F200S G2, Thermo Fisher Scientific) with a 200 kV acceleration voltage. Micrographs were acquired in both bright-field TEM mode and bright-field and high-angle annular dark field (HAADF) STEM modes. Selected area electron diffraction (SAED) patterns were acquired and analysed with the Gatan Digital Micrograph software. EDX spectra were acquired with two windowless Si-drift detectors.

Lamellae were extracted from the worn samples by focused ion beam (FIB) milling (Thermo Fisher Helios 5 CX DualBeam). A 2 μm thick tungsten protective layer was deposited before milling the trenches to protect the area of interest from direct exposure to the ion beam. The lamellae were fine-polished to a thickness of 100 nm using 30 kV @ 0.79 nA (coarse thinning), down to 80 pA (final thinning). The amorphous layer that could have formed due to gallium interaction was removed with a final 5 kV, 5.5 pA polishing step.

2.4.4. Electrochemical corrosion testing

Electrochemical polarization tests were performed on the polished surfaces of the coated samples, prepared as described in Section 2.4.1. A three-electrode cell with the sample as the working electrode (exposed surface area: 1 cm^2), an Ag/AgCl/KCl(sat.) reference electrode, and a Pt mesh as the counter-electrode were filled with 300 mL of a 3.5 % (wt./vol.) NaCl aqueous solution at room temperature under aerated conditions. After the samples had been soaked for one hour, they were polarized from open circuit potential (OCP) to −400 mV vs. OCP and then swept from −400 mV vs. OCP to + 1600 mV vs. OCP at a rate of 0.5 mV/s to record the full electrochemical polarization curve, using a VersaStat 3 potentiostat (Ametek – Princeton Applied Research, USA). Two repeats were performed for each coating type.

The corrosion potential (E_{Corr}) and the corrosion current density (I_{Corr}) were extrapolated from the polarization curves using the Tafel method by fitting linear sections of the anodic and cathodic branches at overpotentials of at least |50| mV away from the equilibrium potential.

The corroded samples were then hot mounted in acrylic resin as described in Section 2.4.3, ground and polished as described in Section 2.4.1, and examined by SEM+EDX to characterize the extent of corrosion damage throughout the section.

3. Results and discussion

3.1. Size distribution, microstructure, and phase composition of the powders

All the HVOF spray-grade powders exhibited similar particle size distributions, as summarized through the 10th, 50th and 90th percentiles listed in Table 4. The powders were only slightly coarser than the nominal −45 + 10 μm range listed in Section 2.2 and were suitable for this thermal spray process. The CGS-grade Al_0(CrMnFeNi) and Cantor

Table 3
High-speed nanoindentation mapping parameters.

Sample	Normal load (mN)	X Size (μm)	Y Size (μm)	Number of indents	Average depth (nm) reached
HVOF Cantor Run2	10	225	225	8100	240
CGS Cantor Run1	10.8	225	225	8100	240
HVOF Al_0(CrMnFeNi) Run3	8	440	184	15360	238
CGS Al_0(CrMnFeNi) Run1	10	250	350	15000	235
HVOF Al_{10}(CrMnFeNi) Run3	8	441	207	17280	236
HVOF Al_{14}(CrMnFeNi) Run3	12	200	200	6400	260

Table 4
Characteristic values (10th, 50th, and 90th percentiles) of the size distributions of the HEBM feedstock powders.

Powder		d_{10} [μm]	d_{50} [μm]	d_{90} [μm]
Cantor	HVOF grade	16	33	59
	CGS grade	14	25	40
	CGS grade (annealed)	18	34	59
Al_0(CrMnFeNi)	HVOF grade	21	37	61
	CGS grade	15	28	48
Al_{10}(CrMnFeNi)		15	31	60
Al_{14}(CrMnFeNi)		15	31	56

powders were finer, as expected, however the particle size distribution of the CGS-grade Cantor powder had slightly coarsened after annealing (Table 4).

The chemical composition obtained by EDX analysis (Table 5) showed that all the powders contained a smaller amount of manganese than was expected, except for the annealed Cantor powder. All other elements respected the nominal proportions in each case. The presence of silicon (Table 5) could have been an artefact. Some particles of the colloidal silica suspension used in the final polishing step (Section 2.2) could have been retained the resin between the powder particles.

SEM micrographs (Fig. 1A, C, E, G) show that the as-milled powder particles had an irregular shape with some cracks. In detail (Fig. 1B, D, F, H), each particle consisted of tightly adherent thin sheets of material. The particles contained a uniform distribution of sub-micrometric dark phases, which were rich in oxygen and occasionally contained traces of sulphur (see Supplementary Material – Figure S1). Accordingly, the chemical analysis by inert gas fusion (Table 5) showed approximately 0.2 – 0.5 wt% oxygen in all powders, as well as 0.17 – 0.18 wt% nitrogen.

Apart from these inclusions, the particles were chemically quite homogeneous, however there were a few areas with different contrasts in backscattered electron imaging (Fig. 1B, D, F, H). Figure S1 in the Supplementary Material indicates that most of those areas were rich in chromium, but there were also areas rich in other elements, such as Ni.

Figure S1A in the Supplementary Material highlights that in the annealed Cantor powder, the individual sheets of metal were no longer clearly identifiable. The dark oxide inclusions were still present (Figure S1B), however a new microstructural feature appeared. This feature consisted of areas based on Cr and Fe, with a brighter back-scattered electron contrast level than the surrounding material, as shown by the Supplementary Material (EDX spectrum in Figure S1B and EDX maps in Figure S2).

The XRD patterns (Fig. 2) revealed that the as-milled powders, including the Cantor and Al_0(CrMnFeNi) compositions, contained the BCC phase, and all the diffraction peaks were very broad. In the annealed Cantor powder (Fig. 2A), by contrast, the diffraction peaks

Table 5
Chemical composition of HEA powders and coatings (mass%, normalized to 100: mean ± standard deviation) measured by EDX analysis on areas imaged at 400 ×, and by inert gas fusion (oxygen, nitrogen) and oxygen combustion (carbon) for the powders.

Element	**Cantor**								
	Nominal	*Powder (as-milled)*	*Powder (annealed)*	*HVOF*			*CGS*		
				Run1	*Run2*	*Run3*	*Run1*	*Run2*	*Run3*
Oxygen	-	0.15 ± 0.07	N/A	11.16 ± 0.24	10.89 ± 0.76	12.19 ± 0.51	1.72 ± 0.04	1.86 ± 0.05	1.63 ± 0.14
Nitrogen	-	0.17 ± 0.01	N/A	-	-	-	-	-	-
Carbon	-	0.28 ± 0.01	N/A	-	-	-	-	-	-
Aluminium	-	0.17 ± 0.02	0.11 ± 0.04	0.11 ± 0.07	0.15 ± 0.09	0.15 ± 0.12	0.20 ± 0.07	0.15 ± 0.06	0.17 ± 0.03
Silicon	-	1.46 ± 0.08	1.15 ± 0.11	0.51 ± 0.04	0.43 ± 0.04	0.50 ± 0.02	0.48 ± 0.03	0.52 ± 0.01	0.52 ± 0.03
Chromium	18.54	20.02 ± 0.04	19.09 ± 0.23	17.38 ± 0.20	17.54 ± 0.27	17.27 ± 0.18	18.84 ± 0.12	18.80 ± 0.05	18.75 ± 0.06
Manganese	19.59	16.96 ± 0.03	19.97 ± 0.34	15.09 ± 0.11	14.76 ± 0.23	14.50 ± 0.23	19.38 ± 0.04	19.68 ± 0.09	19.68 ± 0.10
Iron	19.91	19.00 ± 0.03	19.20 ± 0.06	17.80 ± 0.10	18.08 ± 0.10	17.56 ± 0.13	19.45 ± 0.39	19.19 ± 0.23	19.37 ± 0.21
Cobalt	21.02	20.53 ± 0.10	19.95 ± 0.13	18.88 ± 0.16	19.08 ± 0.16	18.79 ± 0.29	19.83 ± 0.31	19.72 ± 0.13	19.56 ± 0.04
Nickel	20.93	21.26 ± 0.08	20.53 ± 0.23	19.08 ± 0.34	19.06 ± 0.26	19.03 ± 0.24	20.08 ± 0.25	20.07 ± 0.40	20.31 ± 0.19
Element	**Al_0(CrMnFeNi)**								
	Nominal	*Powder*		*HVOF*			*CGS*		
				Run1	*Run2*	*Run3*	*Run1*	*Run2*	
Oxygen	-	0.55 ± 0.01		10.34 ± 0.10	9.95 ± 0.30	8.98 ± 0.12	2.42 ± 0.15	2.25 ± 0.08	
Nitrogen	-	0.18 ± 0.01		-	-	-	-	-	
Carbon	-	0.04 ± 0.01		-	-	-	-	-	
Aluminium	-	0.20 ± 0.06		0.17 ± 0.06	0.23 ± 0.10	0.23 ± 0.11	0.17 ± 0.02	0.20 ± 0.04	
Silicon	-	0.84 ± 0.08		0.41 ± 0.03	0.39 ± 0.04	0.37 ± 0.03	0.32 ± 0.03	0.32 ± 0.03	
Titanium	-	0.14 ± 0.08		0.12 ± 0.04	0.08 ± 0.03	0.09 ± 0.02	-	-	
Chromium	18.81	20.13 ± 0.29		17.34 ± 0.17	17.27 ± 0.12	17.37 ± 0.17	18.91 ± 0.26	19.05 ± 0.1	
Manganese	24.85	18.37 ± 0.35		19.12 ± 0.12	19.06 ± 0.15	19.69 ± 0.14	21.07 ± 0.11	20.49 ± 0.14	
Iron	40.41	43.14 ± 0.26		38.21 ± 0.17	38.52 ± 0.21	38.61 ± 0.18	41.32 ± 0.15	41.89 ± 0.08	
Nickel	15.93	16.41 ± 0.22		14.29 ± 0.12	14.50 ± 0.09	14.66 ± 0.05	15.78 ± 0.13	15.80 ± 0.12	
Element	**Al_{10}(CrMnFeNi)**								
	Nominal	*Powder*		*HVOF*					
				Run1	*Run2*	*Run3*			
Oxygen	-	0.45 ± 0.01		7.75 ± 0.08	8.43 ± 0.12	8.85 ± 0.17			
Nitrogen	-	0.18 ± 0.05		-	-	-			
Carbon	-	0.02 ± 0.01		-	-	-			
Aluminium	5.14	5.77 ± 0.23		5.04 ± 0.03	4.99 ± 0.04	5.10 ± 0.02			
Silicon	-	1.06 ± 0.30		0.20 ± 0.02	0.15 ± 0.03	0.21 ± 0.02			
Chromium	17.85	18.91 ± 0.33		17.77 ± 0.21	17.77 ± 0.04	17.49 ± 0.13			
Manganese	23.57	18.80 ± 0.03		17.56 ± 0.21	17.07 ± 0.27	16.69 ± 0.16			
Iron	38.33	39.33 ± 0.20		37.30 ± 0.19	37.26 ± 0.08	37.30 ± 0.07			
Nickel	15.11	15.49 ± 0.13		14.38 ± 0.14	14.31 ± 0.19	14.35 ± 0.08			
Element	**Al_{14}(CrMnFeNi)**								
	Nominal	*Powder*		*HVOF*					
				Run1	*Run2*	*Run3*			
Oxygen	-	0.54 ± 0.03		6.70 ± 0.14	7.62 ± 0.09	6.34 ± 0.38			
Nitrogen	-	0.18 ± 0.01		-	-	-			
Carbon	-	0.03 ± 0.01		-	-	-			
Aluminium	7.36	7.34 ± 0.03		7.24 ± 0.10	7.22 ± 0.11	7.09 ± 0.10			
Silicon	-	1.07 ± 0.14		0.16 ± 0.02	0.15 ± 0.02	0.19 ± 0.01			
Chromium	17.43	17.93 ± 0.10		16.80 ± 0.19	16.95 ± 0.17	16.86 ± 0.04			
Manganese	23.02	19.43 ± 0.38		17.40 ± 0.33	16.56 ± 0.06	18.22 ± 0.22			
Iron	37.44	39.19 ± 0.39		37.79 ± 0.42	37.59 ± 0.17	37.50 ± 0.21			
Nickel	14.76	14.29 ± 0.05		13.91 ± 0.22	13.90 ± 0.14	13.81 ± 0.07			

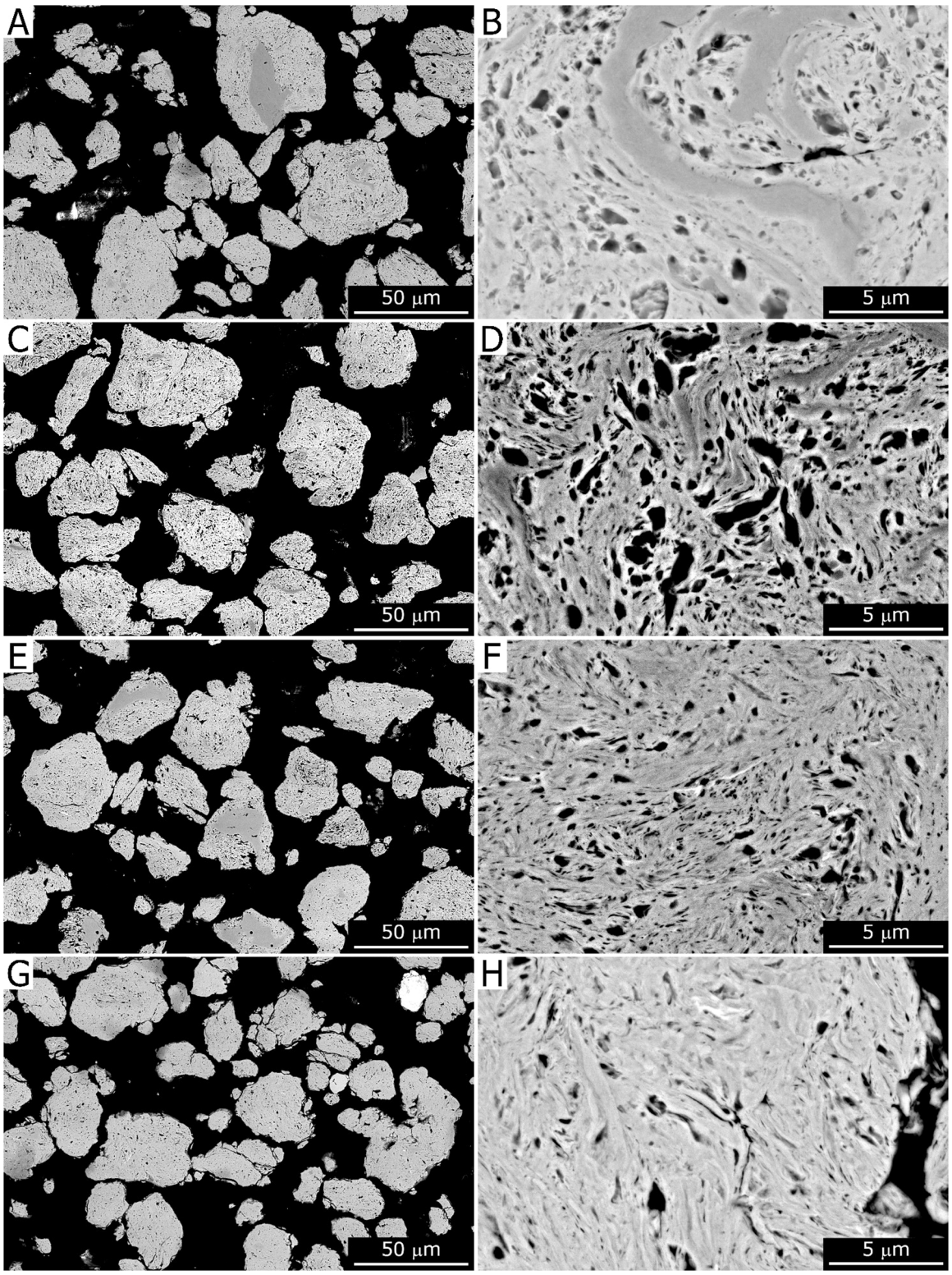

Fig. 1. Cross-sectional SEM micrographs (backscattered electrons) of the Cantor (A, B), Al_0(CrMnFeNi) (C, D), Al_{10}(CrMnFeNi) (C, D), and Al_{14}(CrMnFeNi) (E, F) powders, HVOF spray-grade (A, C, E, G: overviews; B, D, F, H: details).

were substantially sharper; the amount of the BCC peak decreased in comparison to the as-milled powder (Table 6), but weak diffraction peaks of a tetragonal σ-phase appeared, with a quantified amount around 6 wt%.

3.2. Microstructure and chemical composition of the coatings

The HVOF deposition of the four HEA powders resulted in reasonably high deposition efficiencies in the range of 50–60 %, which were nonetheless lower than the ≈ 68 % efficiency obtained with the commercial Stellite-6 powder (Table 7).

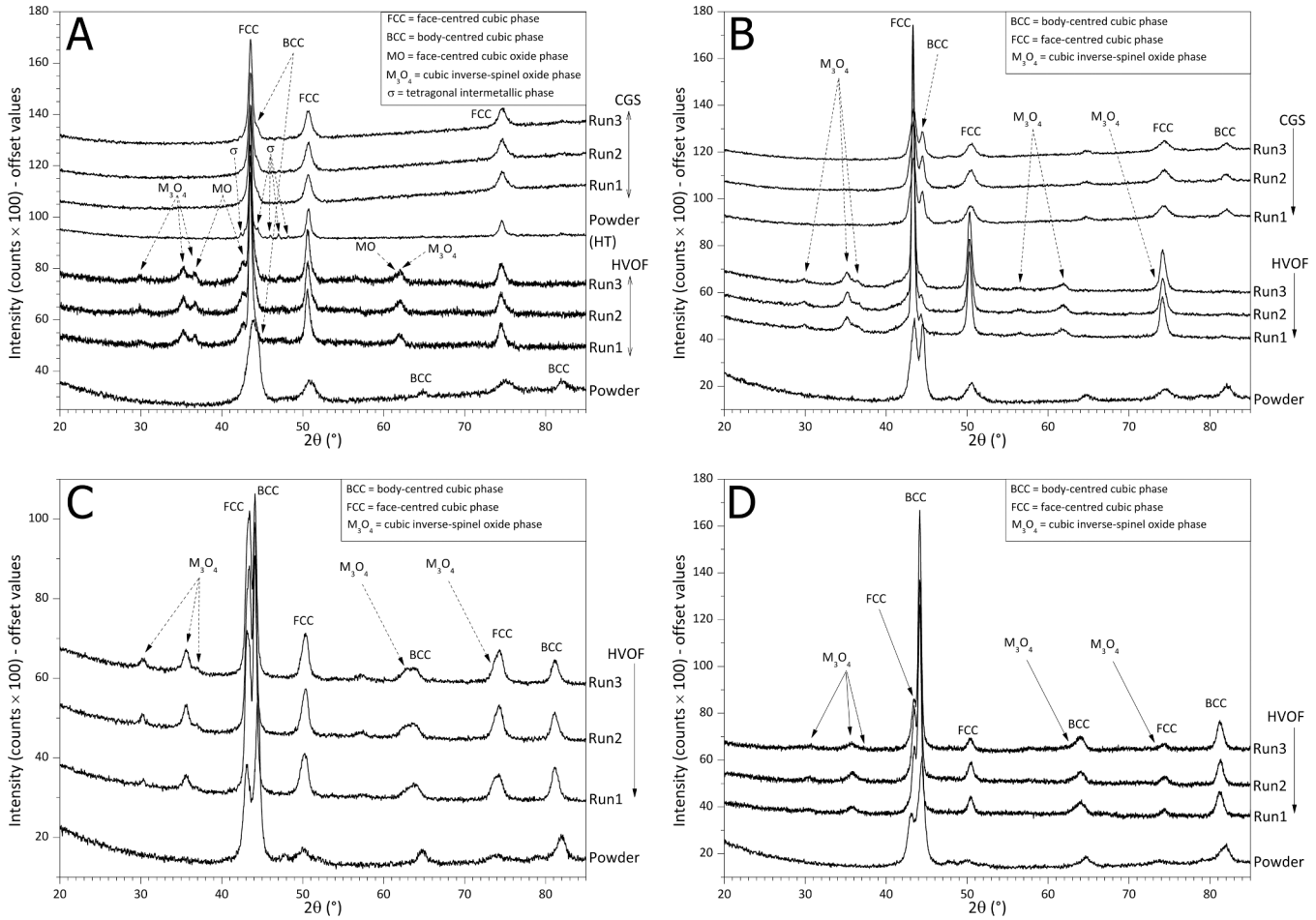

Fig. 2. X-ray diffraction pattens of the feedstock powders and the coatings: Cantor (A), Al_0(CrMnFeNi) (B), Al_{10}(CrMnFeNi) (C), Al_{14}(CrMnFeNi) (D).

The quantitative results from image analysis (Table 7) indicated that the HVOF HEA coatings were all very dense, with porosities often well below 1 % and lower than the Stellite reference, and that the CGS coatings also showed low porosities, which were generally < 1 %. The results also suggested that there were no major differences among the HVOF-sprayed coatings deposited with the same feedstock powder but different process parameters. A qualitative comparison between the microstructures of all coatings (Figures S4 –S7), confirmed this assumption. Therefore, only selected deposition conditions are shown in Fig. 3A-F for ease of comparison.

The CGS Cantor coatings also exhibited identical microstructures, independent of the deposition conditions (Figure S8). Only the CGS Cantor Run2 sample is therefore shown in Fig. 4C, D. In contrast, the CGS Al_0(CrMnFeNi) coatings exhibited increasing signs of erosion damage from Run1 to Run3 (Figure S9). Due to its extreme defectiveness, the CGS Al_0(CrMnFeNi) Run3 sample was discarded from all subsequent analyses and no properties are listed for this material in Table 7. Fig. 4A, B shows the densest of the three CGS Al_0(CrMnFeNi) coatings, deposited using a lower gas stagnation pressure of 6 MPa.

The HVOF-sprayed coatings (Fig. 3B, D, F, H and Figures S4, S5, S6 and S7) showed three distinct types of microstructural features:

- Thin, spread-out lamellae, mostly with a columnar grain structure (Fig. 3B, D, F, H and Supplementary Material – Figures S4, S5, S6 and S7: label 1).
- Less-flattened lamellae, often containing small equiaxed grains (label 2)
- Poorly flattened or non-flattened particles, with coarse equiaxed grains (label 3).

The HVOF-sprayed HEA coatings also contained a substantial amount of oxide inclusions. The image analysis on the SEM micrographs indicated that the oxide fraction ranged from ~20–45 vol% (Table 7). Quantitative EDX analyses (Table 5) consistently showed oxygen content ranged from 6 wt% to 11 wt%. Interestingly, the HVOF-sprayed Stellite coating had a much lower oxide content (4 vol%) and a correspondingly low oxygen content measured by quantitative EDX analysis (2.48 ± 0.19 wt%).

For a more detailed analysis of the oxides in the HVOF HEA coatings, see the Figures S10 – S13. The oxygen content measured by quantitative EDX analyses (Table 5) and the oxide content measured by image analysis (Table 7) were both lower for the Al-containing compositions: Al_{10}(CrMnFeNi) and, even more markedly, Al_{14}(CrMnFeNi) contained fewer inclusions than the Al-free compositions, Al_0(CrMnFeNi) and Cantor. The Supplementary Material shows that there was also a difference in the composition of the oxides. In the Cantor and Al_0(CrMnFeNi) coatings, all oxides exhibited the same level of backscattered electron contrast and contained a mix of all the elements constituting the parent alloy. In the Al_{10}(CrMnFeNi) and Al_{14}(CrMnFeNi) compositions, brighter oxides still consisted of a mixed-cation phase, whereas oxides with a darker contrast were substantially enriched in Al.

In the CGS HEA coatings, the oxide inclusion content could not be reliably measured by image analysis and, therefore, no value is listed in Table 7. However, a qualitative observation of the SEM micrographs in Fig. 4 and Figures S8-S9, as well as the chemical analyses in Table 5, indicated a substantial difference in the degree of oxidation between HVOF and CGS HEA coatings. The oxygen content in the CGS coatings was, in fact, no greater than 2.5 wt% (Table 5), i.e., one order of magnitude lower than in the HVOF coatings, although higher than in the

Table 6
Quantitative phase composition (in wt%) of feedstock powders and coatings by Rietveld refinement of the XRD patterns.

Sample	FCC	BCC	MO	$M^{II}M^{III}_2O_4$
Cantor powder (as milled)	68.2 ± 0.4	31.8 ± 0.5	-	-
*Cantor powder (annealed)**	90.5 ± 0.4	3.5 ± 0.1	0.4 ± 0.1	
Cantor Run1 HVOF	74.3 ± 0.1	-	7.1 ± 0.6	18.6 ± 0.4
Cantor Run2 HVOF	73.2 ± 0.1	-	7.6 ± 0.6	19.2 ± 0.4
Cantor Run3 HVOF	73.8 ± 0.1	-	7.5 ± 0.6	18.7 ± 0.5
Cantor Run1 CGS	95.2 ± 0.3	4.8 ± 0.3	-	-
Cantor Run2 CGS	94.8 ± 0.3	5.2 ± 0.3	-	-
Cantor Run3 CGS	94.9 ± 0.4	5.1 ± 0.3	-	-
Al_0(CrMnFeNi) Powder	66.0 ± 0.3	34.0 ± 0.3	-	-
Al_0(CrMnFeNi) Run1 HVOF	75.8 ± 0.1	1.8 ± 0.1	-	22.4 ± 0.7
Al_0(CrMnFeNi) Run2 HVOF	73.2 ± 0.1	1.5 ± 0.1	-	25.4 ± 0.6
Al_0(CrMnFeNi) Run3 HVOF	77.8 ± 0.7	-	-	22.2 ± 0.7
Al_0(CrMnFeNi) Run1 CGS	80.9 ± 0.1	19.1 ± 0.2	-	-
Al_0(CrMnFeNi) Run2 CGS	81.7 ± 0.1	18.3 ± 0.2	-	-
Al_0(CrMnFeNi) Run3 CGS	81.7 ± 0.1	18.3 ± 0.2	-	-
Al_{10}(CrMnFeNi) Powder	37.3 ± 0.6	62.7 ± 0.2	-	-
Al_{10}(CrMnFeNi) Run1 HVOF	51.7 ± 0.2	34.3 ± 0.2	-	14.0 ± 0.6
Al_{10}(CrMnFeNi) Run2 HVOF	52.7 ± 0.3	26.4 ± 0.2	-	20.9 ± 0.7
Al_{10}(CrMnFeNi) Run3 HVOF	55.9 ± 0.2	23.3 ± 0.2	-	20.8 ± 0.5
Al_{14}(CrMnFeNi) Powder	42.9 ± 0.7	57.1 ± 0.3	-	-
Al_{14}(CrMnFeNi) Run1 HVOF	27.8 ± 0.3	60.7 ± 0.1	-	11.6 ± 0.7
Al_{14}(CrMnFeNi) Run2 HVOF	30.4 ± 0.3	54.1 ± 0.1	-	15.4 ± 0.7
Al_{14}(CrMnFeNi) Run3 HVOF	22.2 ± 0.3	66.2 ± 0.1	-	11.6 ± 0.8

* This powder also contained 5.6 ± 0.4 % σ-phase

corresponding feedstock powders.

SEM micrographs also showed that the original microstructure of the feedstock powders had not altered much in the CGS coatings (Fig. 4). They even retained the chemical inhomogeneities of the initial feedstock powder, as shown by the EDX maps in the Supplementary Material (Figure S14). In detail, two main microstructural regions were identified in the CGS coatings:

- The centre of the CGS-deposited particles retained the original microstructure of the feedstock. In the Al_0(CrMnFeNi) coatings, the different thin metal sheets were thus still identified in the centre of the deposited particles. Some of these areas are labelled "1" in Fig. 4A-B and in the Supplementary Material (Figure S9).
- The boundaries between adjacent bonded particles showed an extensive plastic flow, with evidence of fragmentation of the pre-existing oxide inclusions. Some of the interparticle boundaries with signs of extensive, mutual plastic flow are labelled "2" in Fig. 4B and Figure S9, and by dashed lines in Fig. 4D and Figure S8.

3.3. Phase composition of the coatings

The phase composition of the HVOF-sprayed coatings changed markedly compared to the corresponding feedstock powders. Among the metallic phases, only the FCC was detectable in the HVOF-sprayed Cantor coatings (Fig. 2A, Table 6), with no sign of the BCC phase originally present in the feedstock powder. The HVOF-sprayed Al_0(CrMnFeNi) coatings were predominantly made of the FCC phase with a minor peak of the BCC phase (Fig. 2B, Table 6). The Al_{10}(CrMnFeNi) coatings, on the other hand, exhibited similarly strong peaks for the FCC and BCC phases (Fig. 2C, Table 6) and in the Al_{14}(CrMnFeNi) coatings, the BCC phase was the main one, albeit with ~20–30 wt% of FCC phase (Fig. 2D, Table 6).

Additionally, the XRD patterns of the HVOF-sprayed coatings showed diffraction peaks from oxide phases: spinel-type $M^{II}M^{III}_2O_4$ and cubic MO phases in the HVOF-sprayed Cantor coatings (Fig. 2A, Table 6), and $M^{II}M^{III}_2O_4$ oxides in all of the Al_x(CrMnFeNi) coatings (Fig. 2B-D and Table 6). The quantitative amount of the $M^{II}M^{III}_2O_4$ oxide phase decreased with increasing Al content in the alloy, from $x = 0$ to $x = 14$ (Table 6).

The XRD patterns and the phase composition of the CGS coatings also differed slightly from those of the feedstock powders. Specifically, in the Al_0(CrMnFeNi) coatings, the amount of BCC phase originally contained in the as-milled feedstock powder decreased (Fig. 2B, Table 6), and the main diffraction peak of the FCC phase became a bit narrower.

On the other hand, the narrow XRD peaks of the annealed Cantor powder had widened after CGS deposition (Fig. 2A), the amount of BCC

Table 7
Porosity, thickness and oxide inclusion content (mean ± standard deviation) of all the coatings according to image analysis, and deposition efficiency.

Sample ID		Porosity (vol%)	Thickness [μm]	Deposition efficiency (%)	Oxide Inclusions (vol%)	HV0.3
HVOF	Cantor Run1	0.24 ± 0.05	284 ± 11	54.8	41.8 ± 3.0	531 ± 29
	Cantor Run2	0.21 ± 0.06	281 ± 22	54.2	43.5 ± 3.1	516 ± 29
	Cantor Run3	0.17 ± 0.03	315 ± 23	64.4	45.4 ± 3.1	533 ± 38
	Al_0(CrMnFeNi) Run1	0.69 ± 0.24	305 ± 18	61.0	33.7 ± 3.2	464 ± 28
	Al_0(CrMnFeNi) Run2	0.84 ± 0.33	298 ± 14	59.4	36.8 ± 1.5	435 ± 37
	Al_0(CrMnFeNi) Run3	0.35 ± 0.08	264 ± 14	56.7	29.6 ± 2.0	436 ± 22
	Al_{10}(CrMnFeNi) Run1	0.04 ± 0.02	263 ± 10	59.7	31.7 ± 0.7	487 ± 16
	Al_{10}(CrMnFeNi) Run2	0.02 ± 0.01	259 ± 7	57.5	33.1 ± 1.9	494 ± 35
	Al_{10}(CrMnFeNi) Run3	0.01 ± 0.01	252 ± 8	56.5	33.6 ± 3.7	508 ± 25
	Al_{14}(CrMnFeNi) Run1	0.37 ± 0.22	264 ± 13	52.3	22.2 ± 2.0	501 ± 24
	Al_{14}(CrMnFeNi) Run2	0.46 ± 0.17	252 ± 11	50.4	25.9 ± 2.0	574 ± 31
	Al_{14}(CrMnFeNi) Run3	0.45 ± 0.15	255 ± 12	52.8	19.1 ± 3.1	574 ± 63
	Stellite	0.94 ± 0.51	523 ± 21	68.4	4.3 ± 1.2	584 ± 65
CGS	Cantor Run1	1.26 ± 0.42	360 ± 20	N/A	N/A	542 ± 47
	Cantor Run2	0.84 ± 0.39	298 ± 30			560 ± 20
	Cantor Run3	0.61 ± 0.16	278 ± 27			578 ± 31
	Al_0(CrMnFeNi) Run1	0.53 ± 0.30	280 ± 17			616 ± 22
	Al_0(CrMnFeNi) Run2	0.56 ± 0.50	301 ± 16			608 ± 39

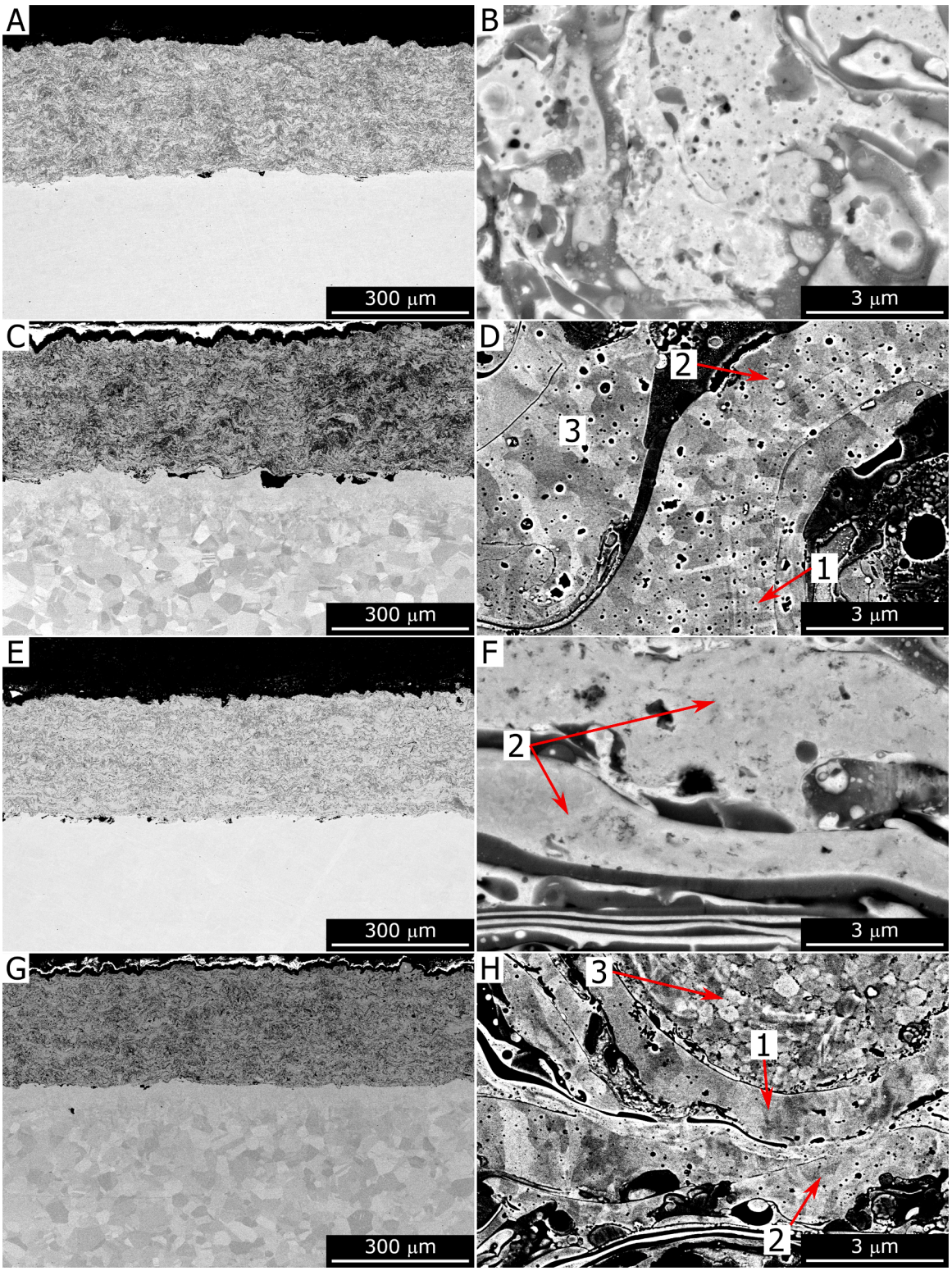

Fig. 3. Cross-sectional backscattered-electron SEM micrographs of the HVOF Cantor Run2 (A, B), Al_0(CrMnFeNi) Run2 (C, D), Al_{10}(CrMnFeNi) Run2 (E, F), and Al_{14}(CrMnFeNi) Run2 (G, H) coatings. Label 1 = columnar grains, 2 = fine equiaxed grains, 3 = coarser equiaxed grains.

phase increased (Table 6), and the peaks of the σ-phase were no longer visible. No diffraction signal from the oxide phases was detected in the XRD patterns of the CGS coatings (Fig. 2).

3.4. Micro- and nano-mechanical properties

3.4.1. Vickers micro-hardness and spherical indentation

The hardness values measured by depth-sensing multi-cycle spherical indentation showed a tendency to increase with the penetration depth (Fig. 5A, C, E, G, I). This is typical of a spherical indentation

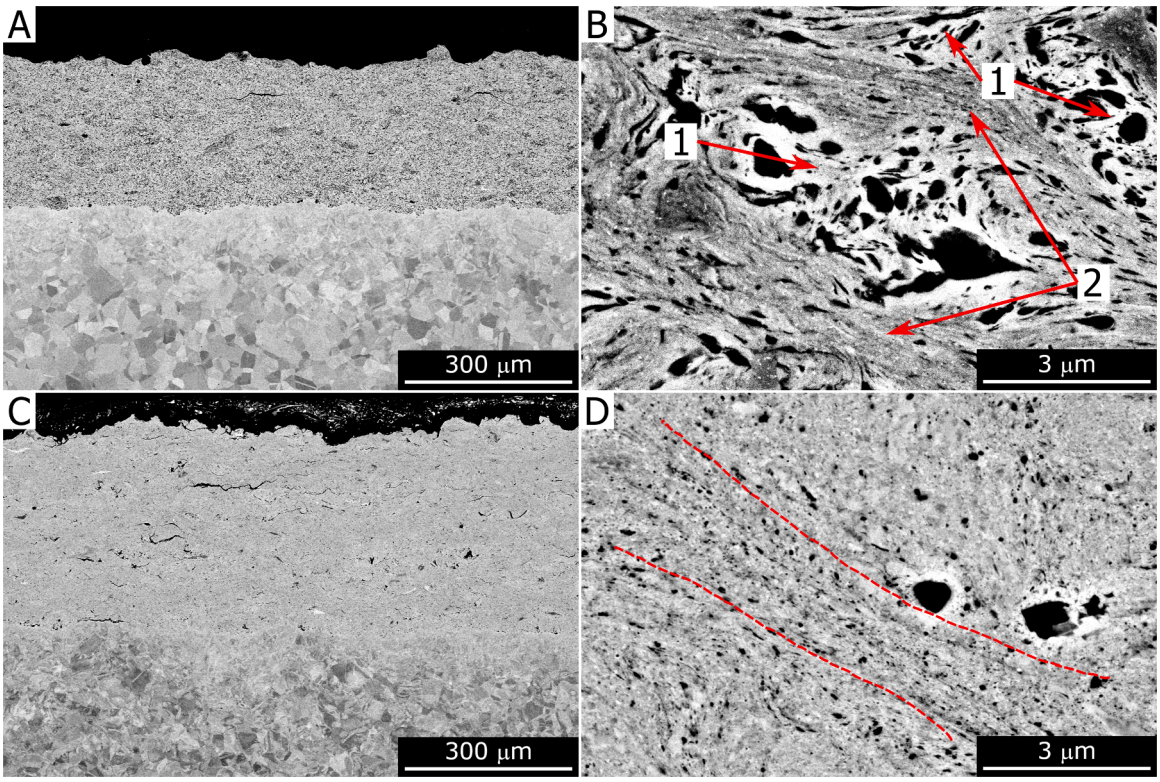

Fig. 4. Cross-sectional backscattered-electron SEM micrographs of the CGS Al_0(CrMnFeNi) Run1 (A, B) and CGS Cantor Run3 (C, D) coatings. In panel B: 1 = undeformed particle core, 2 = interparticle boundaries with extensive plastic flow. In panel D: dashed lines = plastic flow along particle boundaries.

experiment and is due to the non-self-similar nature of the indentation geometry [68]. At high penetration depths, the values tended to stabilize between 7 and 9 GPa for the HVOF-sprayed Cantor (Fig. 5A) and Al_{14}(CrMnFeNi) (Fig. 5G) coatings. However they were lower for the HVOF-sprayed Al_0(CrMnFeNi) (~6–8 GPa, Fig. 5C) and Al_{10}(CrMnFeNi) samples (~7–8 GPa, Fig. 5E). The CGS samples, as well as the HVOF Stellite coating, exhibited somewhat higher indentation hardness (Fig. 5I). All these differences were consistent with the Vickers microhardness measurements (Table 7), which showed the same ranking among the samples, although the hardness values measured by spherical indentation were systematically higher than the Vickers hardness.

Elastic moduli (Fig. 5B, D, F, H) obtained by spherical indentation were around 150–170 GPa for all HVOF-sprayed coatings, 180 GPa - 200 GPa for the CGS coatings (Fig. 5J), and 200 – 220 GPa for the HVOF-sprayed Stellite reference (Fig. 5J).

When extrapolating complete stress-strain curves, a typical work-hardening behaviour was observed, as expected for metallic coatings (Fig. 6). Each data point on the stress-strain curves was the average of the results obtained at the corresponding penetration depth for all the multi-cycle indentations made on each sample, with the corresponding error range. The results exhibited some experimental scatter.

In addition, the data points at the lowest and highest penetration depths deviated from the expected behaviour. This was probably due to slight artefacts related to the imperfect tip geometry, which could not be fully compensated for by the calibration procedure described in Section 2.4.2.2.

Despite these limitations, the data fitted reasonably well to a typical power-law hardening model $\sigma = a \bullet \varepsilon^b$, and two different behaviours were recognized, as shown in Fig. 6A and B respectively. The HVOF-sprayed HEA coatings exhibited a more marked hardening behaviour, with higher values of both the a and b terms in the power-law fit to the data. The HVOF-sprayed Stellite coating and the CGS coatings exhibited less work hardening, with lower values of a and b, as also summarized in Table 8.

3.4.2. *Nanoindentation mapping*

To obtain an even more accurate characterization of the micromechanical properties of the coatings, and probing the "intrinsic" hardness and modulus of the distinct phases, nanoindentation mapping was performed on selected samples as described in Section 2.4.2.3. Because there were no major differences among the coatings obtained with different process parameters, only one sample was tested for each combination of composition and deposition. The very low indentation load meant that it was possible to map the properties of individual phases with high spatial resolution. The results (Fig. 7) showed that the hardness maps reflected the microstructure of the coatings at the micrometre scale fairly accurately. The lamellar microstructure of the HVOF-sprayed coatings is visible in the maps, and it is easy to distinguish the harder oxide inclusions from the softer metallic phases within the lamellae.

Some fluctuations in hardness can be seen at the intra-lamellar level. However, as is shown more clearly in Figure S15, the indentation test sometimes failed to produce usable curves from the oxides.

The data were also visualized in terms of distributive plots, showing the fraction of points with a hardness and elastic modulus within a specified range. By fitting Gaussian curves to the distributive plots, as shown in Figures S15-S16, revealed the "sub-distributions" that characterized distinct "mechanical phases" in the sample. From each Gaussian sub-distribution, the average and the standard deviation of the hardness and elastic modulus of each mechanical phase were extrapolated.

The results in Table 9 show a difference between the HVOF samples, all of which exhibited a sub-distribution with an average hardness > 10 GPa, and the CGS samples, where all of the identifiable sub-distributions had average hardness values < 10 GPa. Overall, either two (HVOF Cantor Run2) or three sub-distributions (all other tested samples) were observed in both the hardness and elastic modulus datasets. There were larger differences between the average hardness values associated with the various sub-distributions of each sample. On

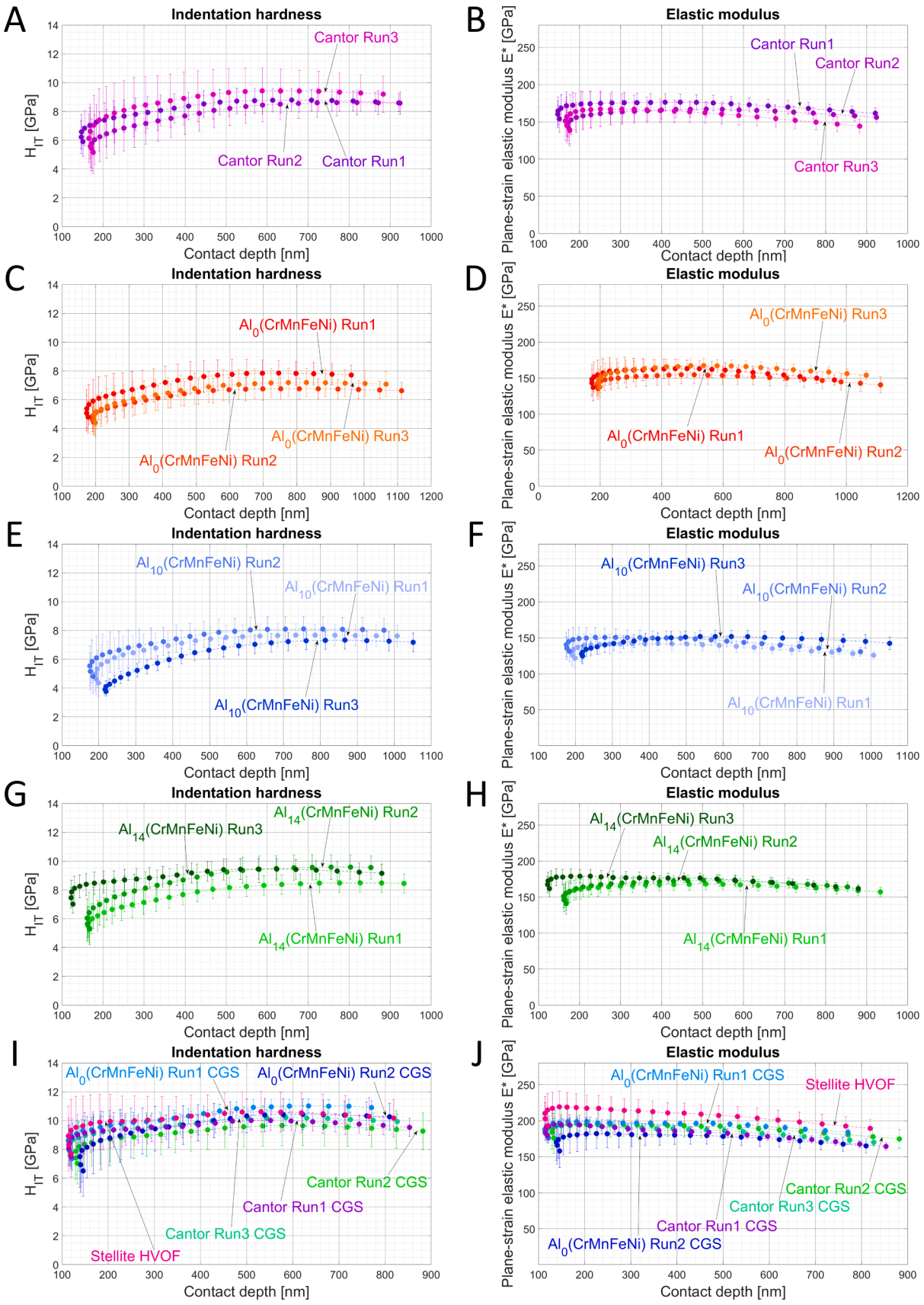

Fig. 5. Indentation hardness (A, C, E, G, I) and plane-strain elastic modulus (B, D, F, H, J) measured by multi-cycle nanoindentation with a spherical tip on the HVOF-spayed Cantor (A, B), Al_0(CrMnFeNi) (C, D), Al_{10}(CrMnFeNi) (E, F), and Al_{14} (CrMnFeNi) (G, H) coatings, on all the CGS coatings and the HVOF-sprayed Stellite-6 reference (I, J).

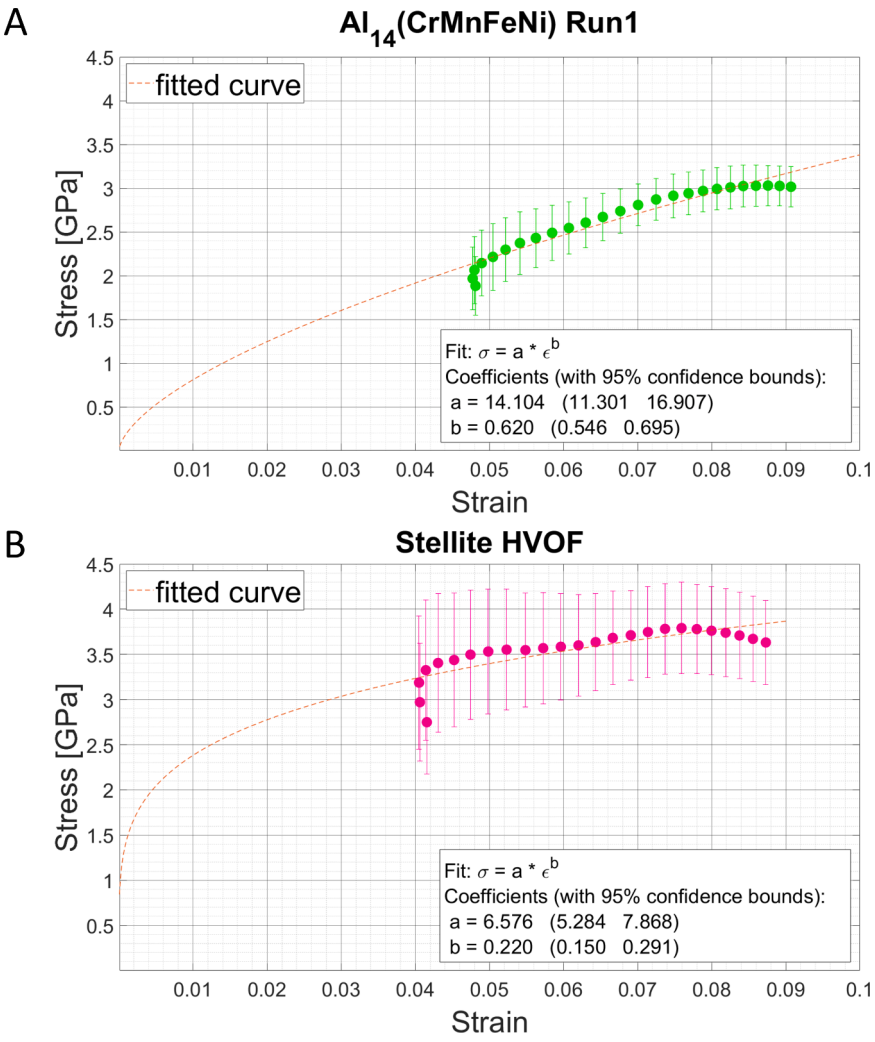

Fig. 6. Example of stress-strain curves extrapolated by multicycle spherical indentation for the HVOF Al_{14}(CrMnFeNi) Run1 (A) and the HVOF Stellite (B) samples.

Table 8
Results of power-law fit of the spherical indentation stress-strain curves for all materials tested: value with lower and upper 95 % confidence bounds in parentheses.

Sample ID		a [GPa]	b
HVOF	Cantor Run1	9.321 (7.421 11.222)	0.436 (0.361 0.512)
	Cantor Run2	16.019 (12.555 19.484)	0.665 (0.584 0.747)
	Cantor Run3	15.756 (9.382 22.131)	0.614 (0.464 0.764)
	Al_0(CrMnFeNi) Run1	12.317 (9.230 15.404)	0.595 (0.501 0.689)
	Al_0(CrMnFeNi) Run2	8.754 (6.674 10.834)	0.527 (0.436 0.618)
	Al_0(CrMnFeNi) Run3	11.894 (8.803 14.984)	0.626 (0.527 0.726)
	Al_{10}(CrMnFeNi) Run1	14.395 (9.345 19.445)	0.671 (0.538 0.804)
	Al_{10}(CrMnFeNi) Run2	13.117 (9.536 16.699)	0.611 (0.508 0.714)
	Al_{10}(CrMnFeNi) Run3	21.325 (14.059 28.591)	0.862 (0.729 0.996)
	Al_{14}(CrMnFeNi) Run1	14.104 (11.301 16.907)	0.620 (0.546 0.695)
	Al_{14}(CrMnFeNi) Run2	12.894 (10.884 14.904)	0.534 (0.474 0.593)
	Al_{14}(CrMnFeNi) Run3	16.790 (13.853 19.728)	0.664 (0.597 0.731)
	Stellite	6.576 (5.284 7.868)	0.220 (0.150 0.291)
CGS	Cantor Run1	5.930 (4.898 6.962)	0.205 (0.142 0.267)
	Cantor Run2	6.913 (5.682 8.143)	0.280 (0.215 0.344)
	Cantor Run3	7.210 (6.138 8.282)	0.272 (0.218 0.325)
	Al_0(CrMnFeNi) Run1	8.292 (7.624 8.960)	0.298 (0.268 0.328)
	Al_0(CrMnFeNi) Run2	12.950 (9.826 16.073)	0.493 (0.405 0.581)

the other hand, the differences between the average elastic modulus values were often smaller than their associated standard deviations.

3.5. Sliding wear testing

3.5.1. Specific wear rates and friction coefficients

The specific wear rates of the HVOF-sprayed HEA coatings in the ball-on-disc test (Fig. 8A) spanned approximately one order of magnitude. These rates were mainly grouped by chemical composition, with no significant effect of the deposition parameters. The specific wear rates increased from the HVOF Cantor coatings, which exhibited the lowest value of 6–8 $\times 10^{-5}$ $mm^3/(N\bullet m)$, to the Al_0(CrMnFeNi) ($\sim$1 $\times 10^{-4}$ $mm^3/(N\bullet m)$), Al_{10}(CrMnFeNi) ($\sim$2–5 $\times 10^{-4}$ $mm^3/(N\bullet m)$), and Al_{14}(CrMnFeNi) ($\sim$5–8 $\times 10^{-4}$ $mm^3/(N\bullet m)$) coatings.

Similarly, the HVOF-sprayed Cantor and Al_0(CrMnFeNi) also caused the lowest degree of wear loss in the counterpart (Fig. 8B), while greater wear losses were caused by the HVOF-sprayed Al_{10}(CrMnFeNi) and Al_{14}(CrMnFeNi) coatings.

In all cases, the specific wear rates of the balls were always at least one order of magnitude lower than those of the coatings. Conversely, the steady-state friction coefficients followed an almost inverse trend (Fig. 8C). The HVOF-sprayed Cantor and Al_0(CrMnFeNi) coatings produced a friction coefficient of around 0.6, whereas the values recorded when testing the HVOF-sprayed Al_{10}(CrMnFeNi) and Al_{14}(CrMnFeNi) coatings were slightly lower and roughly around a value of 0.56.

Among the CGS samples, the Cantor coatings exhibited slightly

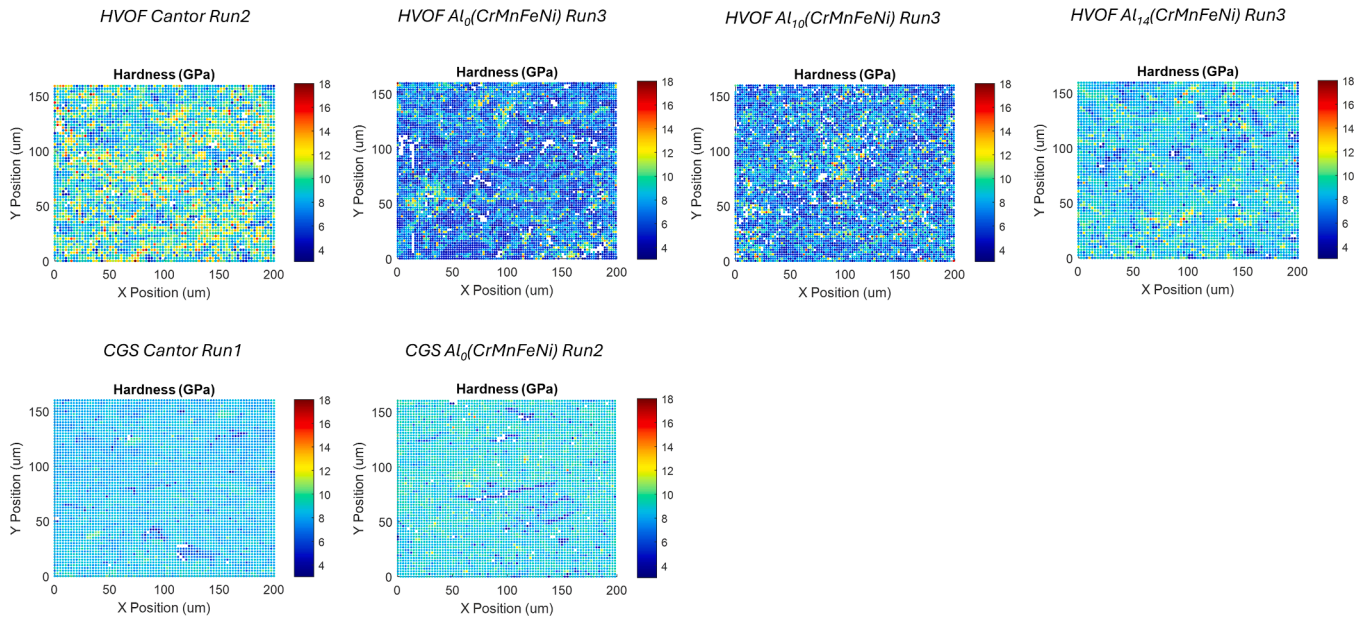

Fig. 7. Hardness maps obtained from high-speed nanoindentation with 2.5 μm spacing between indents. Note: The represented areas are cropped from the actual map sizes, and all samples have been standardized to the same region of interest (ROI) to illustrate comparative differences effectively.

Table 9
Results of least-squares fitting of the nanoindentation data distributions with Gaussian distributions. For each distribution, the results are shown as the average ± standard deviation, and the values in parentheses are the percentages of the overall data that fall within that distribution.

Sample	E_{IT} [GPa]			H_{IT} [GPa]		
	Distribution 1	Distribution 2	Distribution 3	Distribution 1	Distribution 2	Distribution 3
HVOF Cantor Run2	-	184 ± 33 (27 %)	203 ± 25 (73 %)	-	8.61 ± 1.24 (83 %)	12.03 ± 1.26 (17 %)
HVOF Al_0(CrMnFeNi) Run3	247 ± 54 (14 %)	192 ± 51 (79 %)	228 ± 51 (7 %)	5.56 ± 0.95 (45 %)	7.10 ± 1.12 (40 %)	9.65 ± 1.41 (15 %)
HVOF Al_{10}(CrMnFeNi) Run3	135 ± 13 (18 %)	172 ± 21 (72 %)	211 ± 17 (10 %)	4.87 ± 0.92 (22 %)	7.07 ± 1.16 (67 %)	10.45 ± 1.13 (11 %)
HVOF Al_{14}(CrMnFeNi) Run3	168 ± 20 (8 %)	202 ± 18 (89 %)	244 ± 14 (3 %)	6.43 ± 0.92 (15 %)	8.41 ± 0.88 (78 %)	10.57 ± 0.77 (7 %)
CGS Cantor Run1	189 ± 13 (7 %)	210 ± 8 (86 %)	223 ± 10 (7 %)	6.74 ± 0.82 (6 %)	8.12 ± 0.70 (90 %)	9.11 ± 0.51 (4 %)
CGS Al_0(CrMnFeNi) Run2	165 ± 18 (1 %)	230 ± 20 (94 %)	276 ± 17 (5 %)	6.81 ± 0.75 (4 %)	8.81 ± 0.76 (89 %)	9.28 ± 1.11 (7 %)

higher specific wear rates (~1 $\times 10^{-4}$ $mm^3/(N\bullet m)$ than the corresponding HVOF-sprayed coatings, while the Al_0(CrMnFeNi) coatings presented a more similar performance (~1 – 2 $\times 10^{-4}$ $mm^3/(N\bullet m)$), as shown in Fig. 8A. However, the wear losses of the counterparts (Fig. 8B) were higher in both cases, while the friction coefficients, considering the error ranges, were similar, around or close to 0.6 (Fig. 8C).

The specific wear rates of the HVOF and CGS Cantor coatings in this work were very similar to those reported by Silvello et al. [59]. In fact these authors reported sliding wear rates of 6.70 $\times 10^{-5}$ $mm^3/(N\bullet m)$ and 2.80 $\times 10^{-4}$ $mm^3/(N\bullet m)$ for HVOF and CGS Cantor coatings deposited with the same thermal spray systems and under similar processing conditions as in the present work [59].

The HVOF-sprayed Stellite coating was used for comparison purposes. The coating had a lower specific wear rate than all the HVOF and CGS HEA samples (~4 $\times 10^{-5}$ $mm^3/(N\bullet m)$, Fig. 8A). It also produced lower counterpart wear (around 2.3 $\times 10^{-7}$ $mm^3/(N\bullet m)$, Fig. 8B), but produced higher friction (~0.66, Fig. 8C). These results are also consistent with our previous studies on HVOF-sprayed Stellite-6 coatings, where we found analogous values of specific wear rates and friction coefficients under comparable test conditions [49].

The complete friction curves obtained during all the ball-on-disc wear tests run in this work are shown in Figure S17. The latter curves indicated that the HEA coatings, irrespective of the chemical composition and deposition process, quickly reached steady state in almost all of their friction curves. On the other hand the Stellite coating exhibited an initial stage with lower friction followed by a rise to the eventual steady-state regime of higher friction.

Interestingly, the HVOF Cantor Run1 coating, which attained a steady friction regime very early, exhibited approximately the same specific wear rate at sliding distances of 5000 m ((7.78 ± 0.75)× 10^{-5} $mm^3/(N\bullet m)$, Fig. 8A) and 1000 m ((7.69 ± 0.38))× 10^{-5} $mm^3/(N\bullet m)$). In contrast, the specific wear rate of the Stellite coating decreased from (3.94 ± 0.35)× 10^{-6} $mm^3/(N\bullet m)$ after 1000 m (Figs. 8A) to (2.27 ± 0.33)× 10^{-6} $mm^3/(N\bullet m)$ after 5000 m.

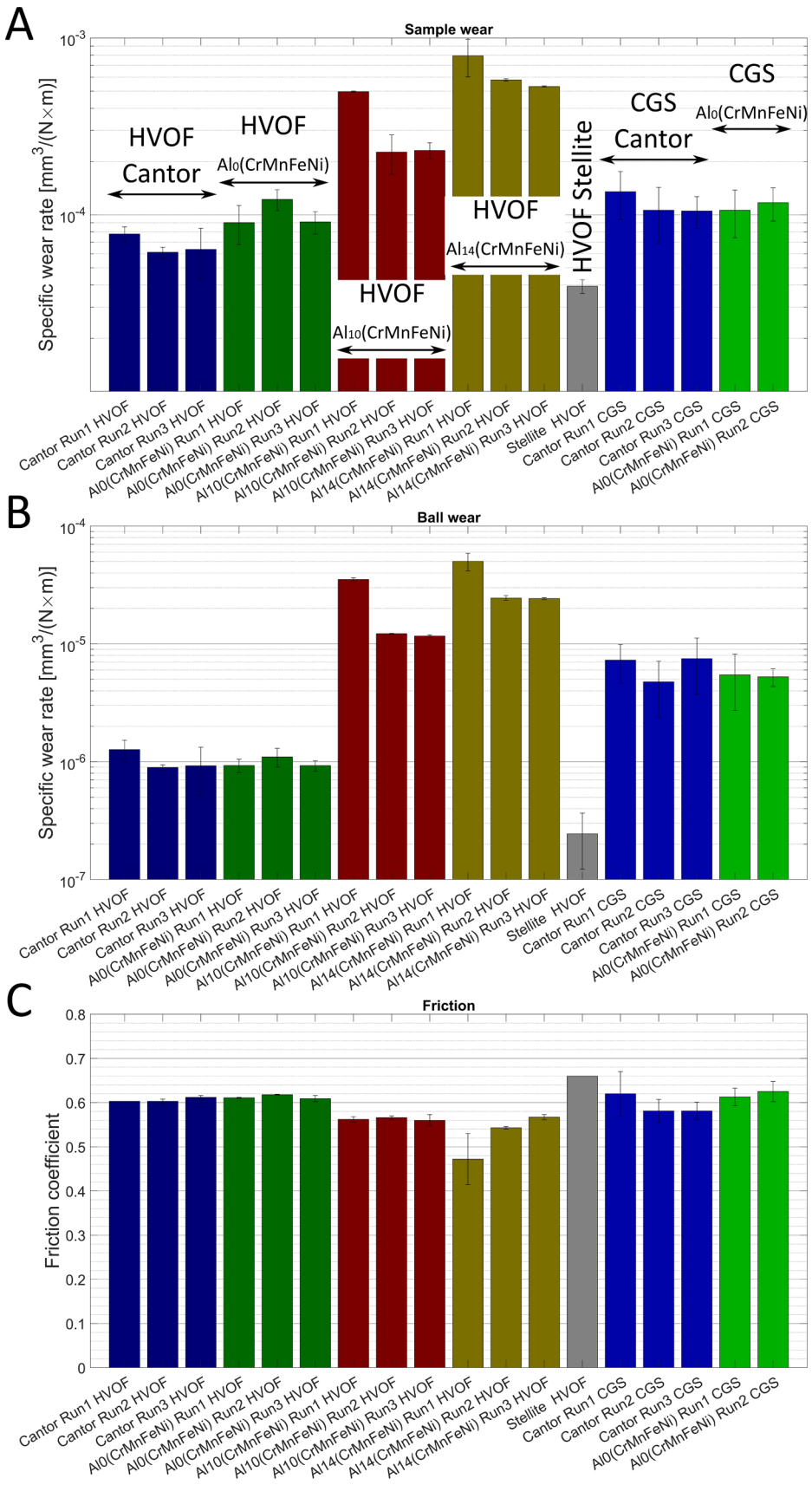

Fig. 8. Quantitative results of the ball-on-disc sliding wear tests: specific wear rates of the coated samples (A) and the balls (B), and steady-state friction coefficients (C). Note: the tests on the HVOF-sprayed Cantor coatings were done over a distance of 5000 m to improve the accuracy of the results on account of the lower wear volume.

3.5.2. SEM and TEM analysis of worn samples

SEM micrographs acquired on the worn surfaces of the HVOF-sprayed Cantor coatings exhibited a mix of ductile tearing (Fig. 9A, B: label 1) and oxidized clusters (recognizable through their darker contrast: Fig. 9A, B: label 2). Analogously, on the surface of the counterpart, shiny patches of transferred metal (Fig. 10A: label 1) and dark clusters of oxidized debris (Fig. 10A: label 2) were observed.

The cross-sectional view of Fig. 11A showed an irregular, sub-micrometric layer of compacted oxidized debris covering part of the worn surface of the HVOF-sprayed Cantor coatings (see arrows). Where the metal surface was exposed, as in Fig. 11B, it had a rough and irregular morphology and showed some evidence of the extrusion of lips of material along the sliding direction (label 1).

However, at other locations along the cross-section of the worn samples, the numerous oxide inclusions contained within the material had emerged on the outer surface (Fig. 11A, B: label 2).

On the surfaces of the HVOF Al_{10}(CrMnFeNi) (Fig. 9C, D) and Al_{14}(CrMnFeNi) coatings (Fig. 9E, F), as well as on the CGS coatings (Fig. 12A, B and C, D), coarser signs of plastic flow were observed, but fewer oxidized clusters. The Supplementary Material (Figure S18) shows in greater detail that the mass fraction of oxygen detected by EDX analyses at various locations along the worn surface was higher in the HVOF Cantor coatings. This decreased progressively in the Al_0(CrMnFeNi), Al_{10}(CrMnFeNi) and Al_{14}(CrMnFeNi) coatings, except for few specific locations corresponding to irregularly distributed oxide clusters. The counterpart surfaces were also covered with shiny patches of transferred metal after sliding wear against the HVOF Al_x(CrMnFeNi) coatings (Fig. 10B-D) and the CGS coatings (Fig. 10E-F).

Correspondingly, on the polished cross-section of the HVOF Al_{14}(CrMnFeNi) coating, two distinctive features were noted. In Fig. 11C, the slightly brighter layer of material indicated by the arrows was probably a sheared lip of metal that was detached, rolled up with other debris in the contact region, and finally re-transferred onto the worn surface. Fig. 11D shows ductile shearing of the metal itself. The metal was plastically dragged along the direction of motion, as highlighted by the dashed line, resulting in the formation of a thin surface layer, marked by the arrows.

Compared with all HEA coatings, the HVOF Stellite coating resulted in a much narrower wear track (Fig. 12E), with no signs of severe ductile tearing. Small pits associated with the loss of lamellar flakes were

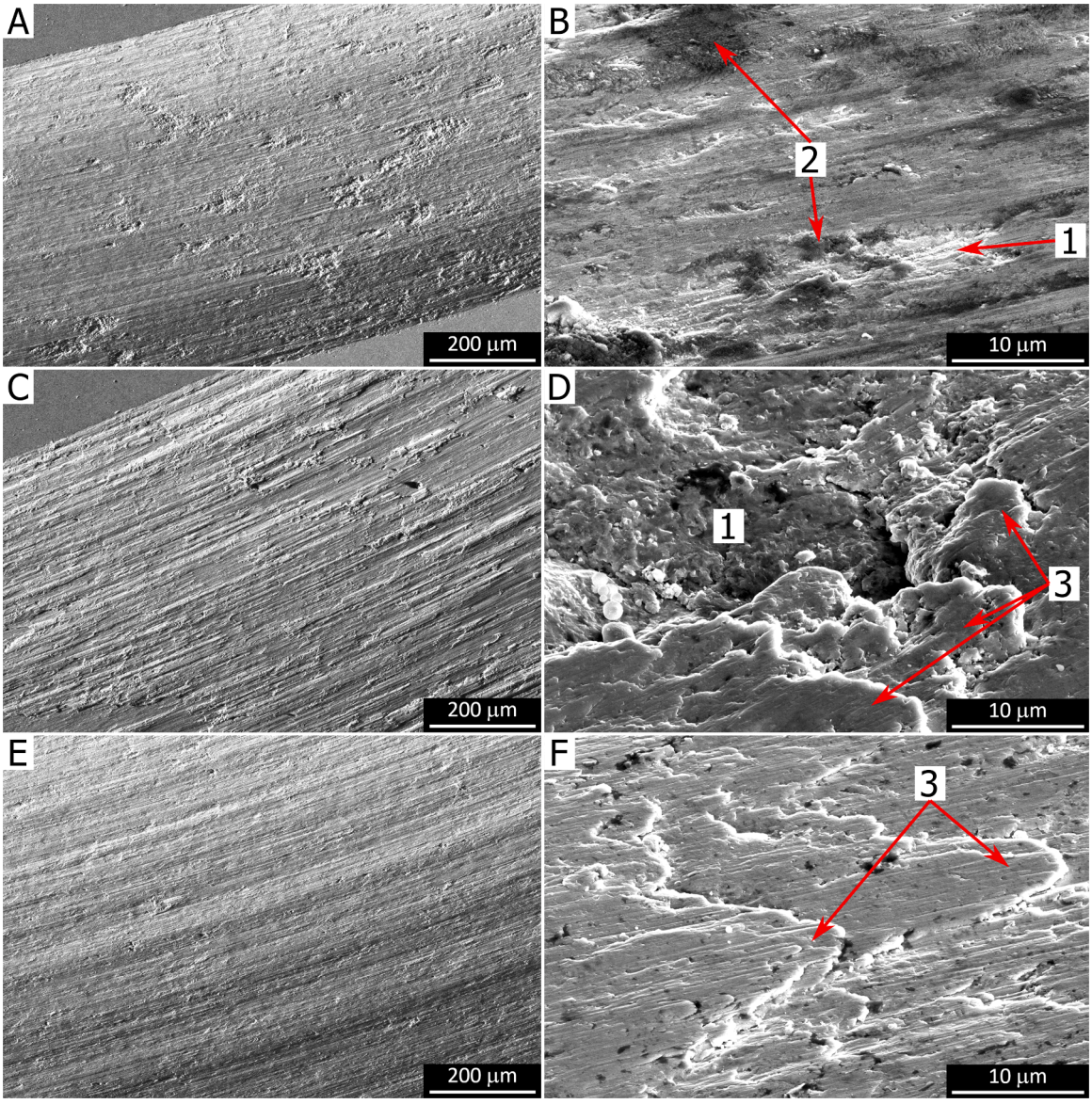

Fig. 9. SEM micrographs (secondary electrons) of the ball-on-disc wear tracks on the HVOF-sprayed Cantor Run2 (A, B), Al_{10}(CrMnFeNi) Run3 (C, D), and Al_{14}(CrMnFeNi) Run3 (E, F) coatings. A, C, E: overviews; B, D, F: details. Labels: 1 = ductile tearing; 2 = tribo-oxidized clusters; 3 = plastic extrusion of lips.

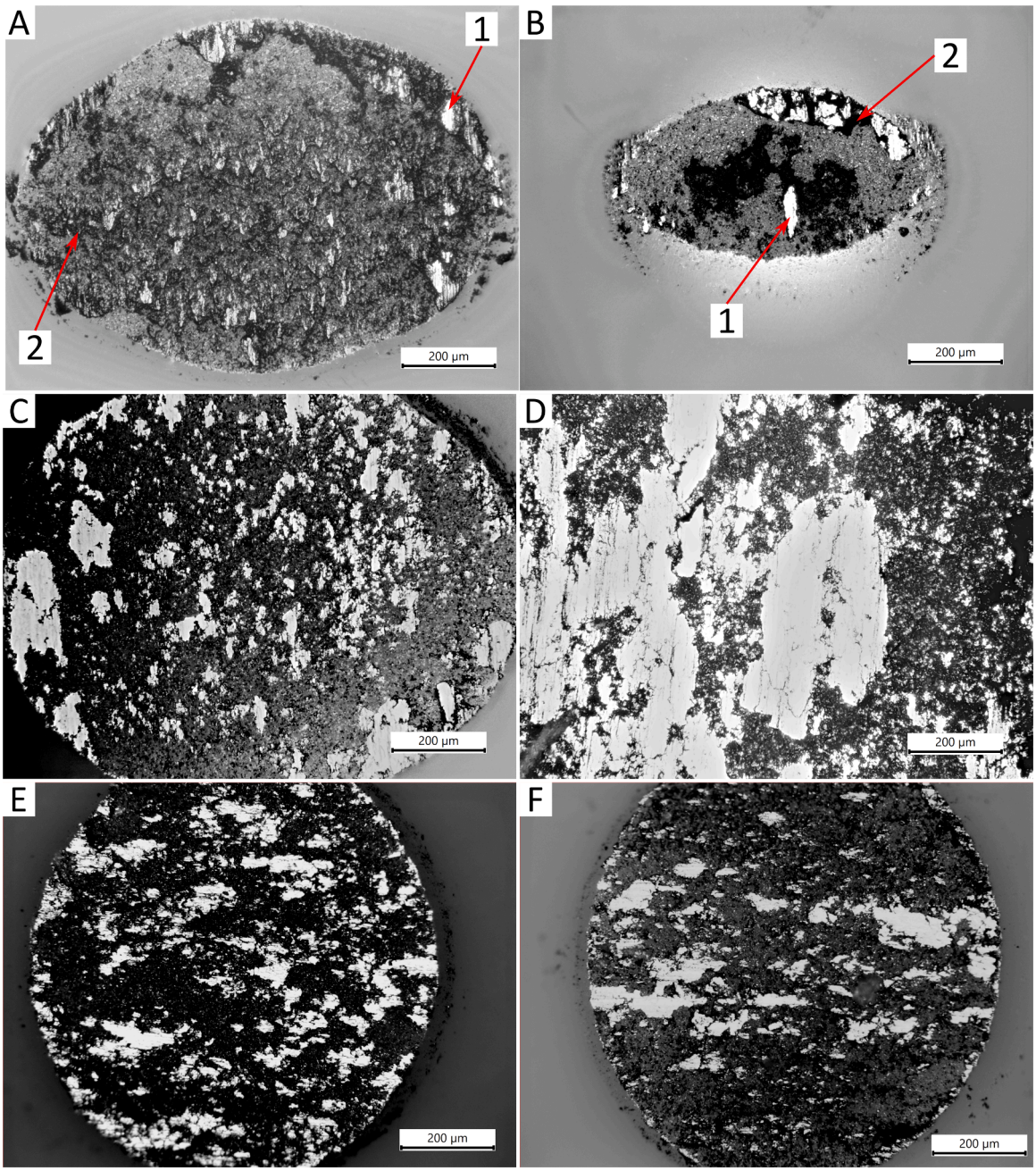

Fig. 10. Optical micrographs of the worn surfaces of the ball counterparts after sliding wear testing against the HVOF-sprayed Cantor Run2 (A), Al_0(CrMnFeNi) Run1 (B), Al_{10}(CrMnFeNi) Run2 (C) and Al_{14}(CrMnFeNi) Run1 (D) coatings, and the CGS Cantor Run1 (E) and Al_0(CrMnFeNi) Run1 (F). Labels: 1 = transferred metal; 2 = tribo-oxidized cluster.

observed, and shallow abrasive grooves (Fig. 12F).

A more detailed analysis of the near-surface tribo-layers was carried out by TEM, using cross-sectional lamellae extracted by FIB from wear tracks that were representative of the two morphologies described above, i.e., the HVOF Al_{14}(CrMnFeNi) Run3 and the HVOF Cantor Run2 samples.

Next to the worn surface of the HVOF Al_{14}(CrMnFeNi) Run3 coating (Fig. 13A), was a 1 µm thick layer with a much finer crystal size than the underlying material. The SAED pattern showed that the base material contained a mix of FCC and BCC phases (Fig. 13C), consistent with the XRD results in Section 3.2. The SAED pattern of the fine-grained surface layer (Fig. 13B) showed more continuous diffraction rings. This was in contrast to the spotty pattern acquired in the interior of the sample, which confirmed the smaller grain size in that layer.

All the diffraction rings from the fine-grained surface layer were indexed exclusively to the FCC phase. This fine-grained layer had been subjected to tearing and delamination. The centre of Fig. 13A showed a longitudinal delamination crack running parallel to the surface, and, on the right-hand side of the same image, the longitudinal crack resulted in the tearing of a portion of material.

A fine-grained layer was also found next to the worn surface of the HVOF-sprayed Cantor Run2 coating (Fig. 14A, B), as outlined by the dashed line in Fig. 14B, but its thickness, as marked by the arrows in Fig. 14B, was no more than 100 nm. The continuous diffraction rings in the SAED pattern of this layer (Fig. 14C) once again confirmed a finer grain size, in comparison with the spotty rings derived from the coarser grains in the interior of the sample (Fig. 14D). The diffraction rings in the SAED patterns of Fig. 14C and D were all indexed to the same FCC

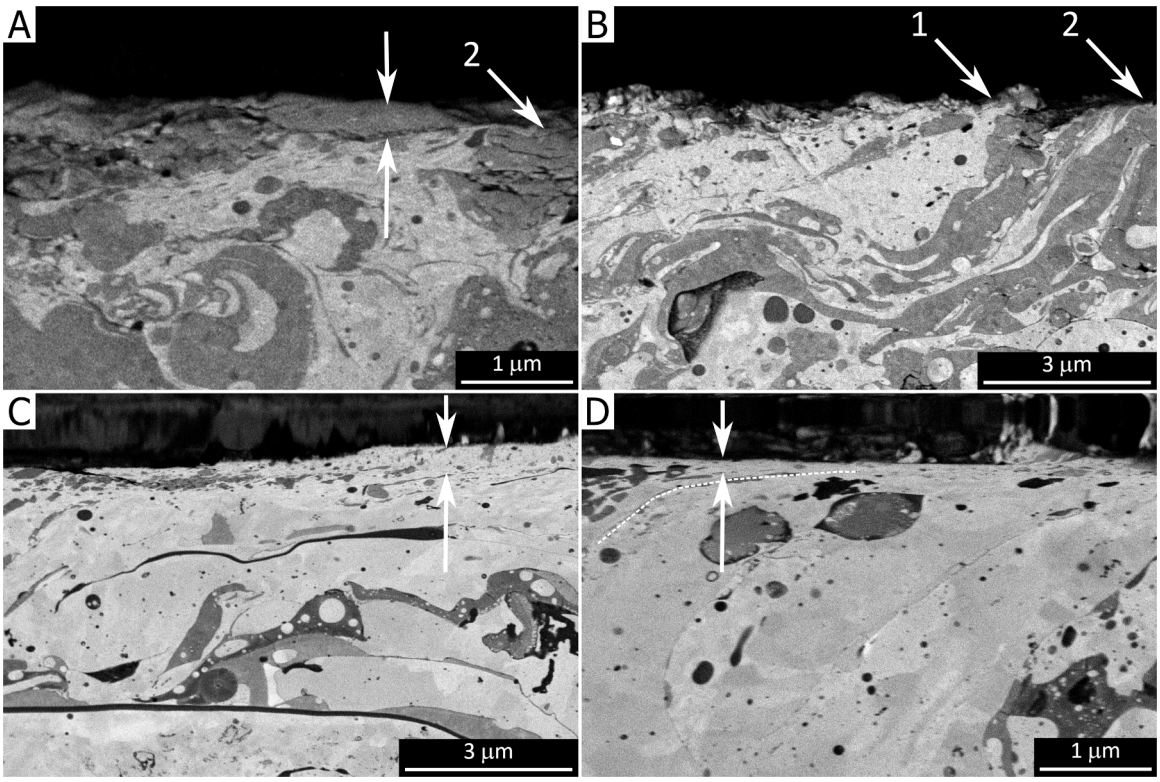

Fig. 11. SEM micrographs (backscattered electrons) of the cross-sections of the ball-on-disc wear tracks on the HVOF-sprayed Cantor Run2 (A, B) and Al_{14}(CrMnFeNi) Run1 (C, D) coatings. The arrows in panel A indicate an oxide tribofilm; those in panel C indicate a plastically deformed layer of retransferred debris; the arrows in panel D indicate a plastically deformed surface layer, with the dashed line indicating the direction of surface plastic flow. Labels: 1 = plastically extruded metal lip; 2 = oxide inclusion exposed to the surface.

structure, consistent with the XRD results (Fig. 2).

3.6. Electrochemical polarization results

The electrochemical polarization curves (Fig. 15) showed that the HVOF-sprayed Cantor coatings had the highest rest potential, and their anodic behaviour featured an initial pseudo-passive stage at current density values in the range of 10^{-6} – 10^{-5} A/cm^2, which lasted up to an anodic overpotential of + 200 mV vs. OCP. This was followed by transpassivation, with a rapid increase in current density up to the order of 10^{-2} A/cm^2.

Regarding the HVOF-sprayed Al_x(CrMnFeNi) coatings, the electrochemical nobility of the sample and the overpotential range of pseudo-passivity both decreased progressively with increasing Al content. The HVOF Al_0(CrMnFeNi) coatings still exhibited some pseudo-passivity, however the current was markedly less stable. Frequent spikes suggested the transient formation of metastable pits, and the breakdown occurred at an overpotential of approximately + 100 mV vs. OCP. The HVOF Al_{10}(CrMnFeNi) and Al_{14}(CrMnFeNi) coatings were even less noble and had an almost continuous anodic activation behaviour with little, if any, pseudo-passivity. The CGS coatings were considerably less noble than their HVOF-sprayed counterparts and exhibited almost no pseudo-passivation behaviour.

These findings were reflected in the values of the corrosion current density and corrosion potential extrapolated from the polarization curves via the Tafel analysis (Fig. 16A and B, respectively). The HVOF-sprayed Cantor and Al_0(CrMnFeNi) coatings in fact exhibited rather low corrosion current densities in the range of 0.4–0.6 µA/cm^2. The corresponding E_{Corr} values were around −150 mV vs. Ag/AgCl/KCl$_{(sat.)}$ for the Cantor coatings and between −220 mV and −270 mV for the Al_0(CrMnFeNi) coatings. The HVOF-sprayed Al_{10}(CrMnFeNi) and Al_{14}(CrMnFeNi) coatings exhibited increasing corrosion current densities, although rarely exceeding 1 µA/cm^2. The CGS coatings had notably less noble E_{Corr} values, and corrosion current densities of approximately 1 µA/cm^2 (Cantor) or even 9–10 µA/cm^2 (Al_0(CrMnFeNi)).

The HVOF-sprayed Stellite reference was electrochemically less noble than all HVOF-sprayed HEA samples (Fig. 15, Fig. 16B), and its corrosion current density was higher, at around 1.5 µA/cm^2 (Fig. 16A). However, it exhibited a wider pseudo-passive stage, spanning an anodic overpotential range of around 350 mV, and after the breakdown of the initial pseudo-passivity range, the current density increased only up to the level of 5×10^{-4} A/cm^2 (Fig. 15). A further increase occurred only toward the end of the test, at the highest applied overpotentials.

The cross-sections of the corroded samples provided in Fig. 17 showed that, at the end of the anodic polarization stage, the HVOF-sprayed coatings developed a severely damaged layer on their upper portion (Fig. 17A, B). In the CGS coatings (Fig. 17C, D), the corrosion attack was at least as extensive and, when examined in detail (Fig. 17D), followed the same patterns of plastic deformation as in the as-deposited material (cf. Fig. 4B for the same composition).

4. Discussion

4.1. Microstructural and phase evolution during processing

The structural and microstructural analyses of the powders (Section 3.1) and the coatings (Sections 3.2 and 3.3) showed that each technological process, from HEBM to the different thermal spray processes, had distinctive effects on the HEAs.

The as-milled powders, including the Cantor and Al_0(CrMnFeNi) compositions, contained some BCC phases (Fig. 2, Table 6), although they were expected to only consist of a single FCC phase. As we reported in [69] for hardmetal compositions with HEA matrices, the most likely

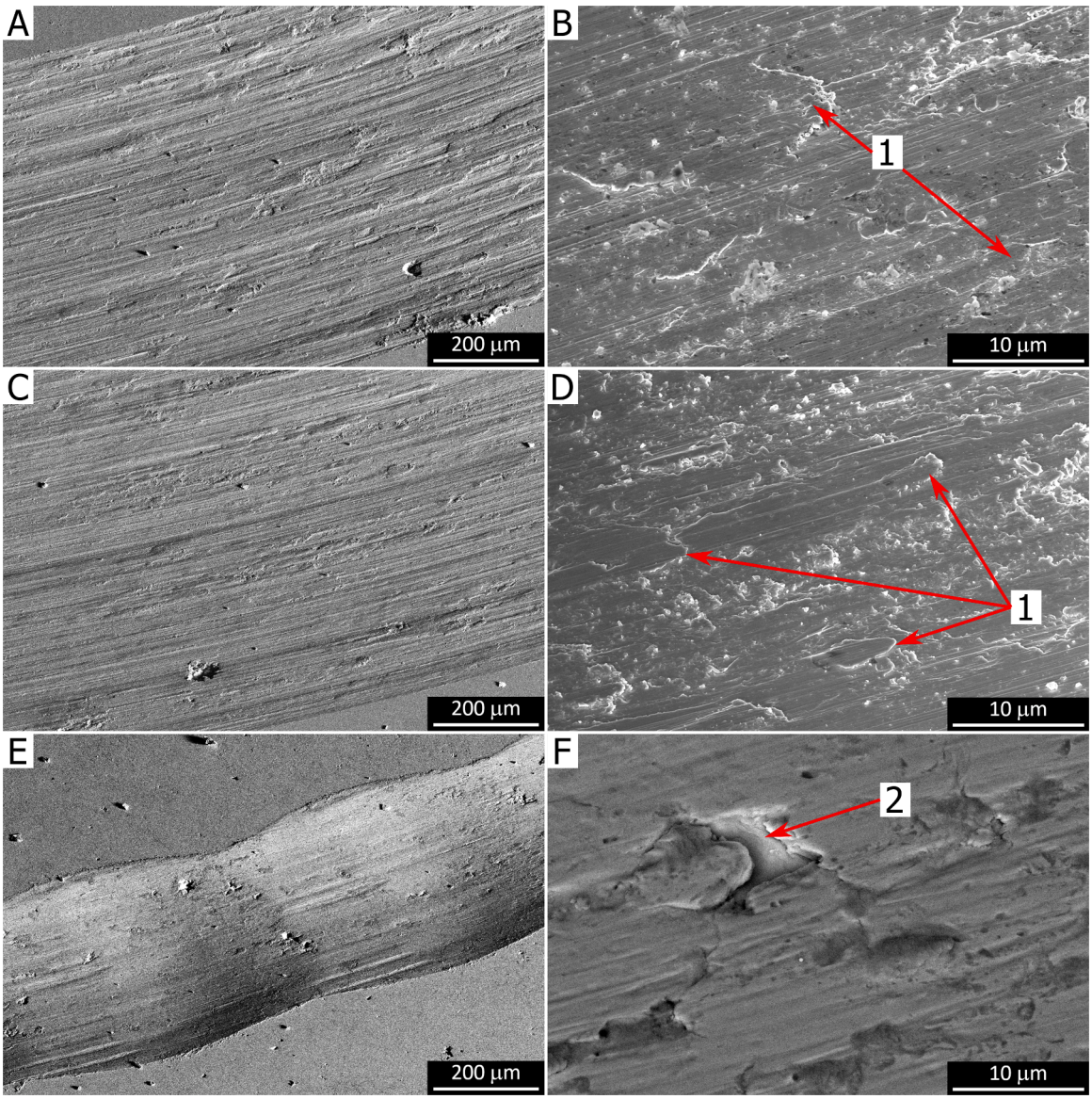

Fig. 12. SEM micrographs (secondary electrons) of the ball-on-disc wear tracks on the CGS Cantor Run2 (A, B) and Al_0(CrMnFeNi) Run2 (C, D) coatings, and the HVOF-sprayed Stellite coating (E, F). A, C, E: overviews; B, D, F: details. Labels: 1 = plastic extrusion of lips; 2 = micro-pit.

explanation is that the lattice strains induced by the HEBM process, which were also responsible for the width of the powder diffraction peaks in Fig. 2, destabilized the more densely packed FCC phase, which led to the formation of the BCC phase. In fact, the morphology of the as-milled powders described in Section 3.1 showed signs of extensive plastic deformation resulting from the cold working process exerted by HEBM. The welded, deformed metal sheets and the microcracks found in several particles both point to a dynamic process of plastic deformation, fracturing, and welding of the material during HEBM. In addition, some of the BCC diffraction signals might have been due to the Cr-rich areas in the powders, since Cr has a BCC lattice. In fact, some residual inhomogeneities in the feedstock materials indicated that, while interdiffusion among the elemental constituents was quite extensive during the HEBM process, it was not complete. Cr, in particular, did not seem to completely diffuse into the other constituents. On the other hand, no FCC phase was expected in the Al_{10}(CrMnFeNi) and Al_{14}(CrMnFeNi) compositions, however there was a FCC phase likely due to the occasional presence of Ni-rich areas as shown in the Supplementary Material.

Inclusions of oxides and, occasionally, sulphides (Fig. 1 and Supplementary Material – Figure S1) were also observed. These could have originated from the fracturing of the scales on the surface of the raw material particles during the HEBM process.

More oxygen and sulphur might also have been taken up during the HEBM process itself. The milling vials were filled with inert gas and sealed, however traces of contaminants such as oxygen might have been present, which might have reacted with the freshly exposed, plastically deformed metal surfaces that were continuously produced by the dynamic welding – fracturing described above.

Annealing of the CGS-grade Cantor powder resulted in the disappearance of the severely cold worked microstructure seen in the SEM micrographs, since the individual sheets of metal were no longer clearly identifiable. During the 3h-long annealing, the system started to evolve toward the equilibrium phase mix of the Cantor alloy at 600 °C, although the evolution was not complete. In fact, the amount of the BCC phase decreased substantially, while 6 wt% of σ-phase appeared (Fig. 2A, Table 6), which corresponded to the Cr,Fe-rich phase observed by SEM and EDX (Figures S1B and S2). However, according to thermodynamic equilibrium calculations performed with ThermoCalc and provided in Figure S3, the equiatomic Cantor alloy should consist of approximately 31 % σ-phase and 69 % FCC phase at 600 °C, whilst the

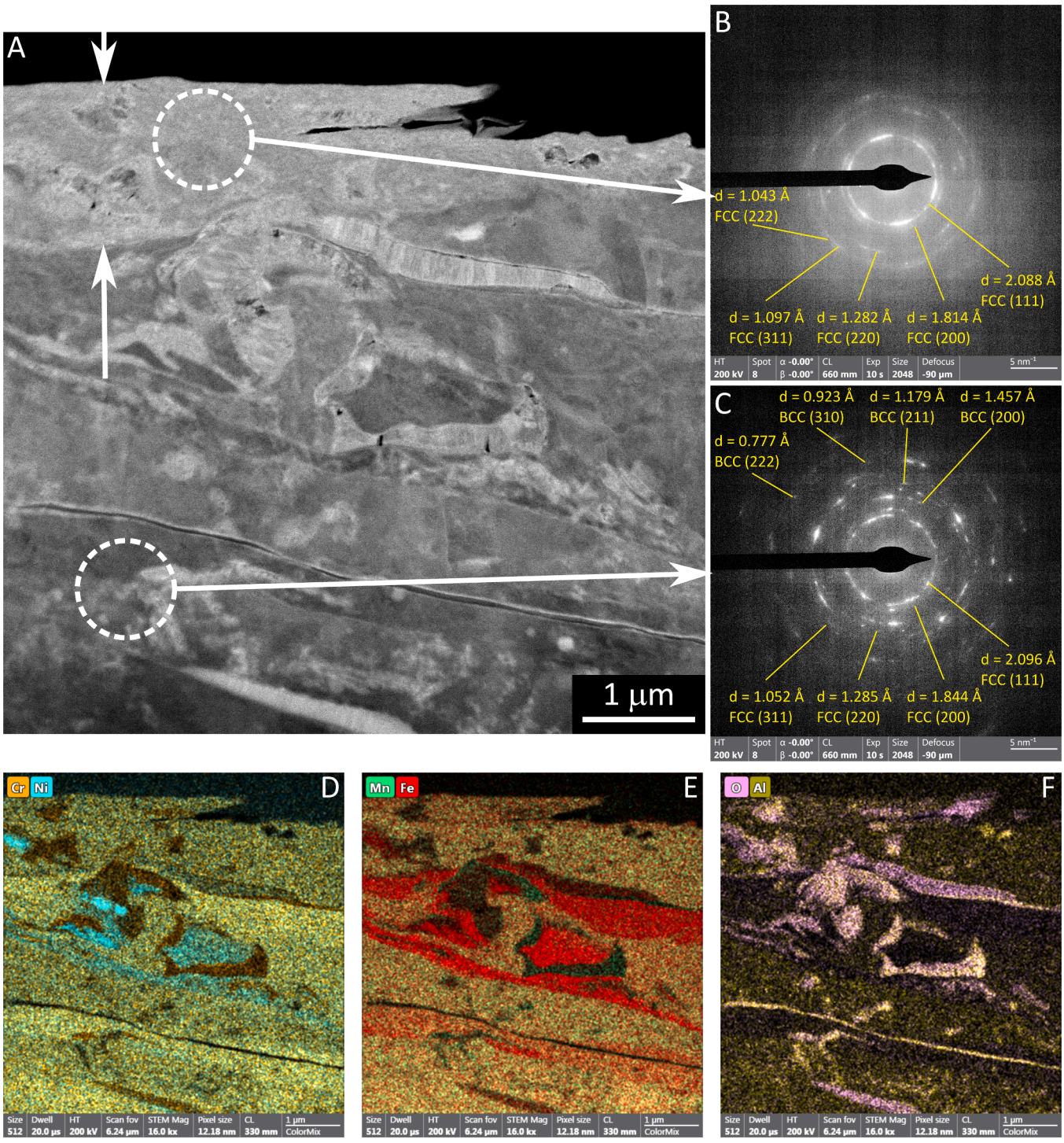

Fig. 13. TEM analysis of the cross-section of a ball-on-disc wear track on the HVOF-sprayed Al_{14}(CrMnFeNi) Run3 coating. A: High-Angle Annular Dark Field (HAADF) STEM micrograph; B, C: Selected Area Electron Diffraction (SAED) patterns acquired next to the worn surface and at a depth below the surface, respectively; D-F: EDX maps of Cr, Ni (D), Mn, Fe (E), O, and Al (F).

BCC phase should not be present. Small peaks of an MO oxide phase appeared in the XRD patterns of the annealed Cantor powder because, also for this oxide phase, annealing reduced the amount of lattice defects resulting from HEBM. Sharper diffraction peaks thus emerged from the background. The diffraction signal from the oxide phase was, in fact, probably due to the same inclusions initially seen in the as-milled powder. There was no indication that the feedstock particles oxidized further during the 600 °C-annealing process in an inert atmosphere. The coarsening of the particle size distribution of the Cantor powder after annealing (Section 3.1 and Table 4) also indicated that some sintering had occurred during annealing. Another difference between the as-milled and the annealed Cantor powders, noted in Section 3.1, was the slightly higher fraction of Mn in the latter. It is unlikely that there was an uptake of Mn during annealing. Because the annealed powder was produced in a distinct milling batch, there was probably a degree of compositional variability from batch to batch.

By heating most of the particles above or, at least, close to their melting points, the HVOF spraying erased the original microstructure of

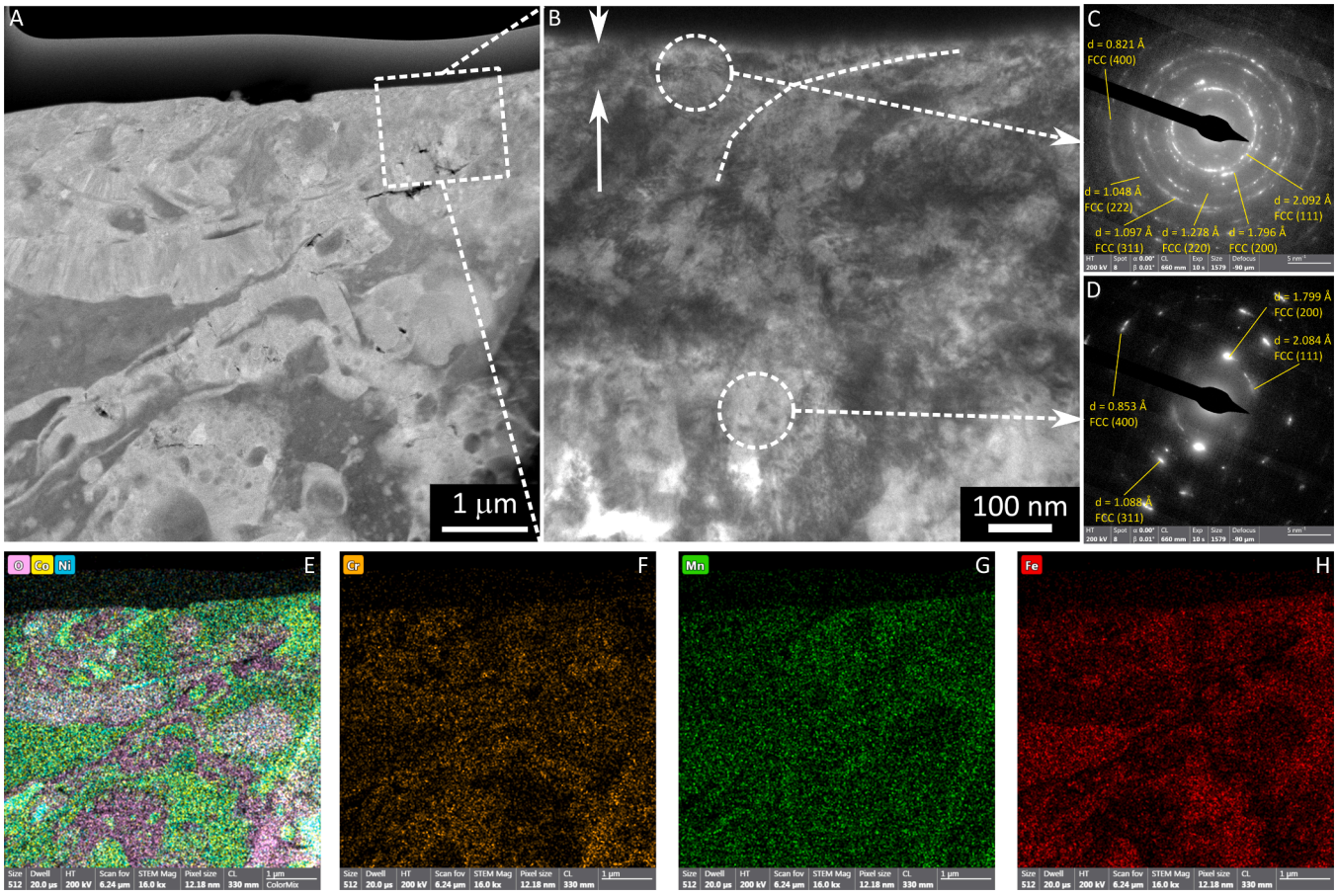

Fig. 14. TEM analysis of the cross-section of a ball-on-disc wear track on the HVOF-sprayed Cantor Run2 coating. A: High-Angle Annular Dark Field (HAADF) STEM micrograph; B: TEM detail of the area marked in panel A; C, D: Selected Area Electron Diffraction (SAED) patterns acquired next to the worn surface and at a depth below the surface, respectively; E-H: EDX maps of O, Co, Ni (E), Cr (F), Mn (G), and Fe (H).

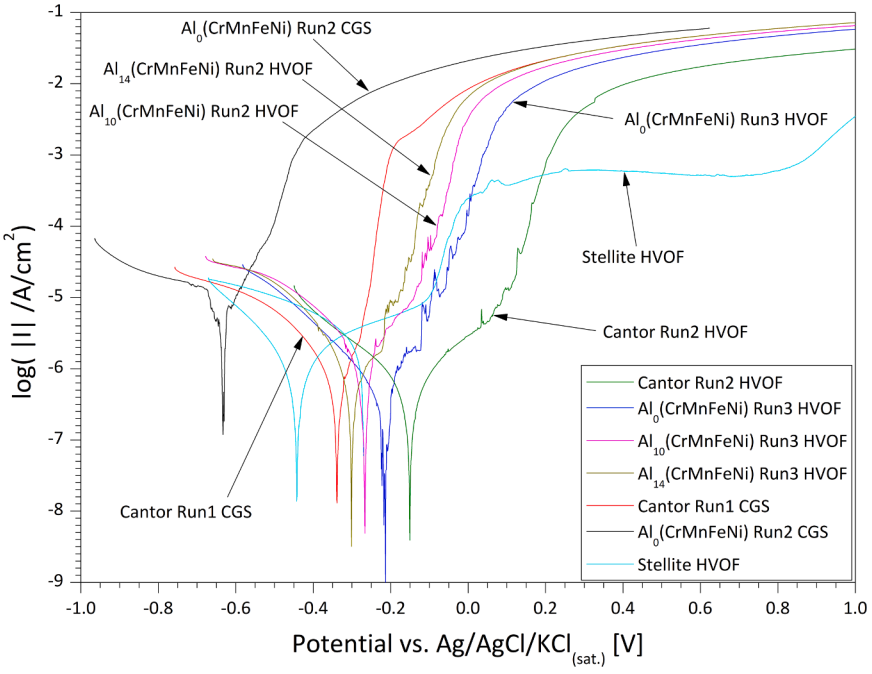

Fig. 15. Representative electrochemical polarization curves for each material / deposition process combination explored in this work.

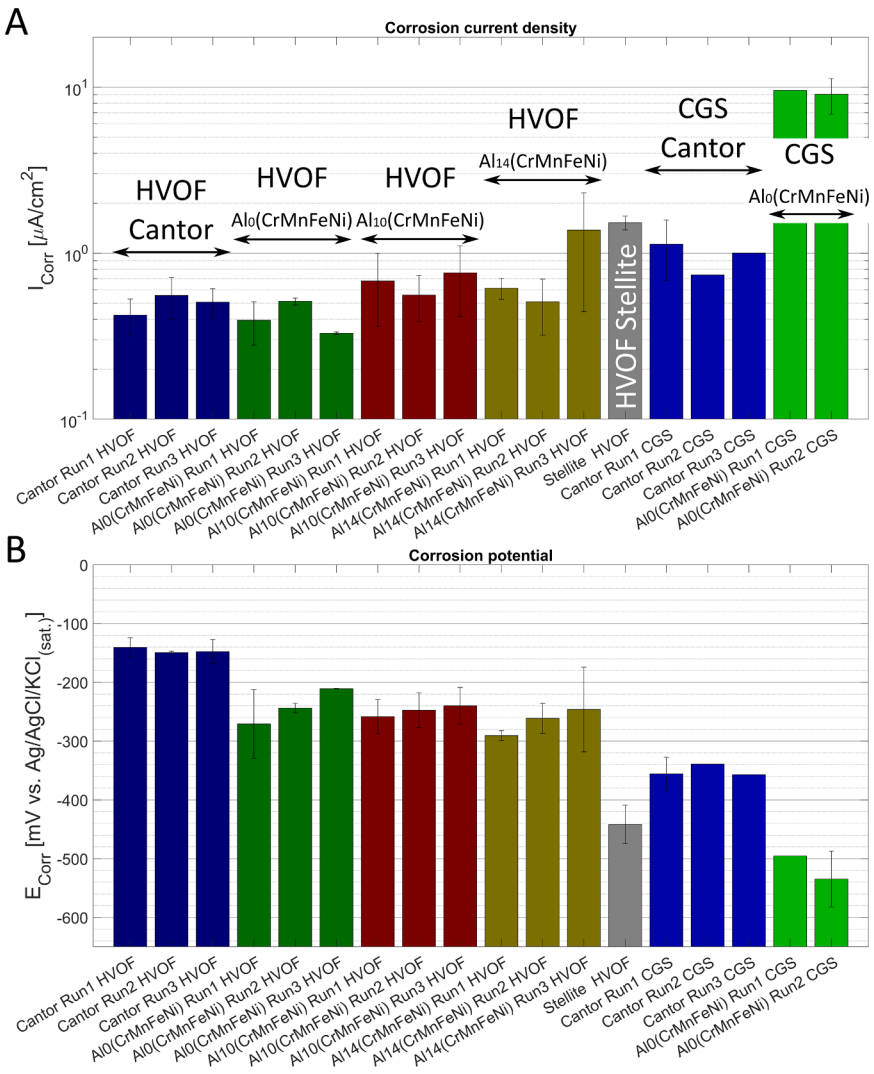

Fig. 16. Corrosion current density (I_{Corr}) and corrosion potential (E_{Corr}) values for all coatings.

the feedstock powder entirely.

As noted in Section 3.2, the HVOF-sprayed coatings consisted of:

1) Thin, spread-out lamellae originating from particles that impacted onto the target surface in a fully molten state. In fact, their columnar grain structure reflected heterogeneous nucleation at the interface with the underlying material. This was followed by a grain growth driven by a mostly unidirectional heat flow across the thickness of the flattened particle toward the underlying material.
2) Less flattened lamellae, which were indicative of a lower impact velocity and/or incipient re-solidification before impact. In these conditions, the heterogeneously nucleated grains originating at the interface with the underlying material could not grow into the central part of the melt before the latter reached a sufficiently high degree of undercooling to trigger homogeneous nucleation. Many, slow-growing, homogeneously nucleated grains thus gave rise to the fine, equiaxed microstructure seen in these less-flattened areas.
3) Poorly flattened or non-flattened particles, which originated from the in-flight solidification of molten metal droplets before they impacted on the substrate. This entailed a slower cooling rate than the solidification process described at point 2 above, which resulted in homogeneous nucleation inside the molten particle, but at a lower degree of undercooling. The nucleation rate was therefore lower in comparison to the grain growth rate, thus resulting in fewer, coarser grains. Some other non-flattened particles might have also derived from unmolten particles that had re-crystallized after being heated close to their melting points.

Because most of the powder particles experienced melting and solidification at relatively high rates during the HVOF-spraying process, the phase composition of the HVOF coatings approached that expected for the respective material at the solidus point (described in Section 2.1). It should be noted that materials such as the Cantor alloy, when produced by conventional methods such as casting, usually develop a dendritic microstructure where Cr is enriched in the interdendritic phase because of solute segregation [70,71]. However, there were no signs of solute segregation in the HVOF-sprayed Cantor coatings, and especially in the fully spread-out lamellae (Fig. 3B and Supplementary Material: Figure S4 and Figure S10). It has long been known [72] that, in thermally sprayed splats, the very high cooling rates produce a planar, instead of dendritic, crystal growth mechanism, which is consistent with the columnar grains seen in the flattened splats, and complete solute trapping.

On the other hand, the Al_{10}(CrMnFeNi) and the Al_{14}(CrMnFeNi) coatings developed a two-phase mix, with a combination of BCC and FCC phases, as also shown in the SEM+EDX analyses (Fig. 3F, H and Supplementary Material – Figures S12, S13). In fact, in the Al_{10}(CrMnFeNi) and the Al_{14}(CrMnFeNi) coatings, the metallic splats contained two distinct phases with different backscattered electron contrast levels and a different Al content, which presumably corresponded to the FCC

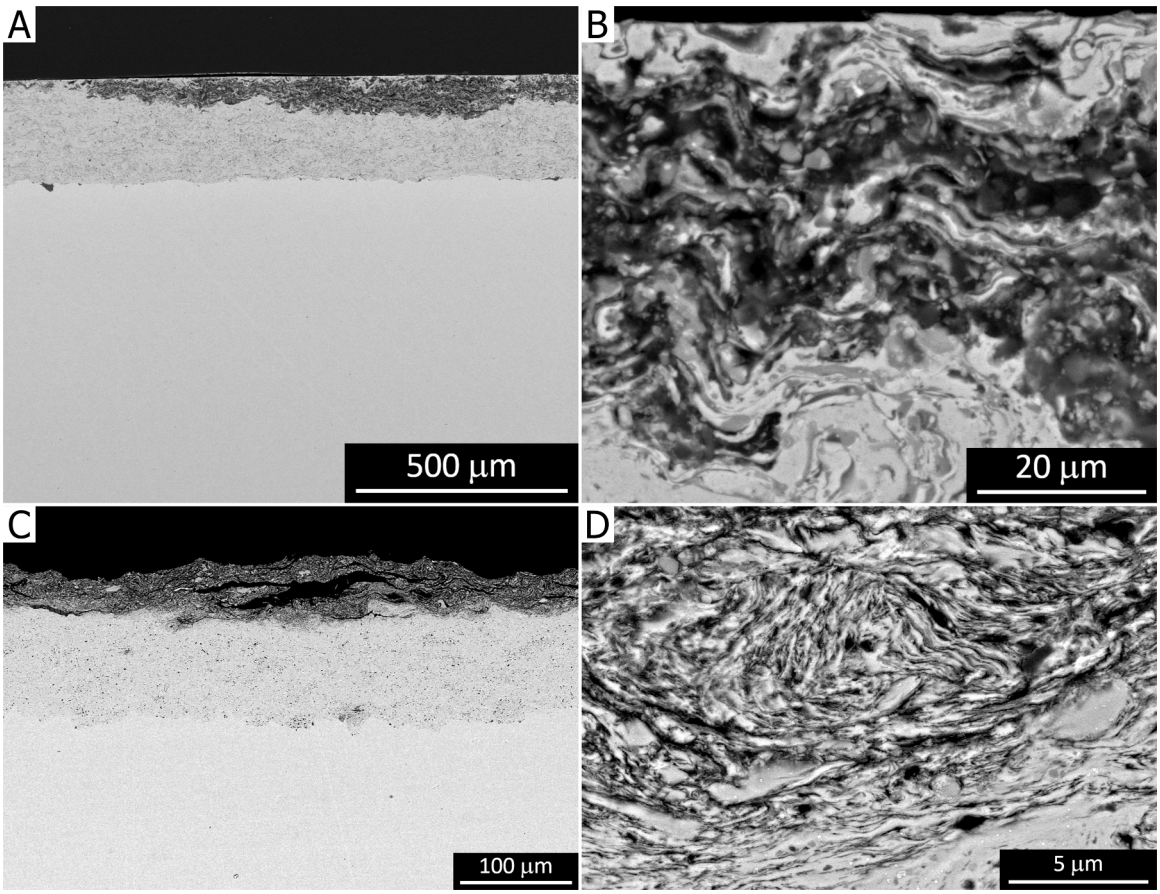

Fig. 17. SEM micrographs (backscattered electrons) of the cross-sections of the HVOF Al_{14}(CrMnFeNi) Run1 (A, B) and CGS Al_0(CrMnFeNi) Run1 (C, D) coatings after the electrochemical polarization test: overviews (A, C) and details (B, D).

(Al-poor) and BCC (Al-rich) phases. Thus, even at very large cooling rates, the high thermodynamic tendency to develop a BCC phase resulted in its formation. However, probably because of the rapid cooling, slight discrepancies were shown between the phase composition of the Al_{10}(CrMnFeNi) and the Al_{14}(CrMnFeNi) coatings and the phases expected at the solidus point under thermodynamic equilibrium. For example, in the Al_{14}(CrMnFeNi) coatings, the BCC phase was the main one, but some 20–30 wt% of the FCC phase was present (Fig. 2D, Table 6), which would not have been expected thermodynamically.

The other major effect of the HVOF deposition was the formation of a substantial amount of oxide inclusions. The inclusions had various morphologies (Fig. 3 and Supplementary Material: Figures S4-S7), most of which were different from the tiny, slightly irregular oxides in the feedstock particles (Fig. 1 and Supplementary Material: Figures S1-S2). Large, elongated inclusions were observed around the lamellae, and submicrometric spherical inclusions within the lamellae. Deshpande et al. [73] described in detail how oxides with these morphologies arise during thermal spraying. They showed that spherical intra-lamellar inclusions derive from in-flight oxidation, whilst elongated stringers can appear both during flight and, more prominently, immediately after flattening of the lamella. Some of the intra-lamellar inclusions in the HVOF-sprayed coatings do not have a perfectly spherical shape. These may correspond to the pre-existing inclusions in the feedstock powder, part of which might not have melted during spraying.

The amount and nature of the oxide phases formed during the HVOF spraying process was affected by the composition of the alloy. As described in Section 3.2, increasing the amount of Al in the parent alloy resulted in a decrease in the oxygen content measured by quantitative EDX analyses (Table 5) and the oxide content measured by image analysis (Table 7).

The composition of the oxides themselves also changed. In the Cantor and Al_0(CrMnFeNi) coatings, all oxides contained a mix of all the elements constituting the parent alloy, which was consistent with the spinel-type $M^{II}M^{III}_2O_4$ phase observed in their XRD patterns. The XRD pattern of the Cantor coating also exhibited a cubic MO phase. Because cubic MO oxides can host a mix of transition-metal cations, this phase was also consistent with the oxide composition observed by EDX. Part of the MO phase might have been contributed by the oxide inclusions pre-existing in the feedstock powder. In fact, although the diffraction signal from the oxide inclusions was not visible in the as-milled powders, in the annealed Cantor powder, where all diffraction peaks were rendered sharper and more easily identifiable, an MO phase appeared. It was however in a far smaller amount than in the HVOF-sprayed coating (Table 6), indicating that oxidation during the HVOF process was still the main contributor to the formation of the MO oxide.

In the Al_{10}(CrMnFeNi) and Al_{14}(CrMnFeNi) compositions, the oxide inclusions with brighter backscattered electron contrast levels, containing a mix of transition metal cations, were again consistent with the spinel-type $M^{II}M^{III}_2O_4$, however the oxides with a darker contrast were substantially enriched in Al. Many of these Al-rich oxide inclusions were in the form of thin, elongated stringers around the metallic splats, as shown in the Supplementary Material – Figure S12 (spectra 4, 5, and 6) and Figure S13 (spectrum 4). By enclosing the metal phase, these Al-rich oxides might have exerted a protective effect, thus limiting the diffusion of oxygen toward the interior of the particles, and explaining the lower overall amount of oxide inclusions and lower content of oxygen in these coatings.

However, in the XRD patterns of the Al_{10}(CrMnFeNi) and Al_{14}(CrMnFeNi) coatings (Fig. 2C, D), there was no distinct diffraction signal of the Al-rich oxides themselves. Either their amount was below

the detection limit of the XRD technique, and/or the lower atomic mass of aluminium compared to the other transition metal elements meant that Al-based oxides had lower X-ray scattering efficiency than the mixed oxides and the surrounding metallic phase. Thus their diffraction peaks were unable to emerge above the background of the XRD patterns.

There was a considerably lower oxide content in the HVOF-sprayed Stellite coating. This could be partly attributed to the oxide inclusions in the HEA feedstock powders themselves, as seen in Section 3.1. However, as previously discussed, most of the oxide inclusions in the HVOF-sprayed HEA coatings developed during the spraying process. The process parameters employed for the HVOF deposition of the HEA coatings and the Stellite coating did not differ substantially. Therefore, it can be hypothesized that HEA powders obtained by HEBM were especially sensitive toward oxidation.

On the one hand, this could be due to their composition. Compared to Stellite-6, the HEA compositions were richer in elements with a high affinity for oxygen, such as chromium and manganese. On the other, the sensitivity might also be related to the particular features of HEBM powders, which, compared to a gas atomized powder, consisted of more irregular particles with microcracks. Hence, their specific surface area was greater than that of the spherical, gas-atomized Stellite-6 powder particles. In addition, the HEBM materials contained large microstrains, as testified by the breadth of the powder XRD peaks. A correspondingly high content of lattice defects could therefore have made the material more reactive. In fact, some HVOF-sprayed HEA coatings obtained from gas-atomized powder, such as the Cantor coatings by Kamnis et al. [74] and CrFeCoNi-based coatings by Löbel et al. [75], exhibited much fewer oxide inclusions. Kamnis et al. [74] reported an oxide inclusion content measured by image analysis that was roughly comprised of between 1 vol% and 10 vol%, i.e. much lower than in the present samples. However, Patel et al. found 18 wt% oxygen, i.e. even more than in our samples, in a HVOF-sprayed Cantor coating also obtained from a gas-atomized powder [76]. More research is therefore needed to ascertain whether, and to what extent, the powder manufacturing process affects the oxide content in HVOF sprayed HEA coatings.

The CGS coatings also had a much lower oxide inclusion content than the HVOF HEA coatings, which was logically consistent with the solid-state nature of this process. The SEM micrographs showed that the original microstructure of the feedstock powders was much less altered in the CGS coatings, including the morphology of the oxide inclusions, as seen by comparing the CGS coatings (Fig. 4B, D and Supplementary Material: Figure S8 and Figure S9) and the corresponding feedstock powders (Fig. 1A-D and Supplementary Material: Figure S1 and Figure S2). The pre-existing inclusions were thus carried over, unaltered, into the CGS coatings. However, the amount of oxygen in the CGS coatings was higher than in the feedstock powders (Table 5), indicating that also during the CGS process, some additional oxidation took place.

Unlike the HVOF coatings, there were no clear morphological cues to differentiate the pre-existing and the newly formed oxides in the CGS coatings, probably because the oxides formed during HEBM and CGS underwent a similar process. During CGS, a very thin oxide shell could have formed around the heated particles, which was then fragmented by plastic deformation upon impact, just like the pre-existing shells around the initial particles which were broken during HEBM.

In fact, the main microstructural change that occurred to the feedstock powders after CGS, as described in Section 3.2, was the plastic flow along the boundaries of the bonded particles. These plastically deformed areas existed both at the bottom and at the top of each particle (label “2” in Fig. 4B and Figure S9, and dashed lines in Fig. 4D and Figure S8). This means that, when a particle impacted onto another one, plastic flow happened both at the bottom of the impacting particle and the topmost part of the impacted one. This was evidence of adiabatic shear instability, the key process by which cold-sprayed particles bond to each other and to the underlying substrate [77].

This was particularly important not only with the annealed Cantor powder, but also with the as-milled Al_0(CrMnFeNi) powder in order to enable the deposition of dense Al_0(CrMnFeNi) coatings, because, as mentioned in Section 2.2, the Al_0(CrMnFeNi) powder could not be annealed prior to CGS deposition. Annealing at sufficiently high temperatures to relieve the cold-worked microstructure of the as-milled Al_0(CrMnFeNi) powder also led to the formation of too much σ-phase. This resulted in an increased hardness of the particles and worsened the deformability upon solid-state impact, as verified through our preliminary experiments.

Another consequence of the lack of melting of the powder particles during CGS was that the particles retained their chemical inhomogeneities, as shown by the EDX maps in the Supplementary Material (Figure S14). However, even CGS, which is a fully solid-state process, did not leave the phase composition of the feedstock material unaffected. In the Al_0(CrMnFeNi) coatings, the amount of BCC phase originally contained in the as-milled feedstock powder decreased (Fig. 2B, Table 6), and the main diffraction peak of the FCC phase became slightly narrower.

The latter finding was in contrast to the generally accepted wisdom that, because of plastic deformation upon impact, the XRD peaks of CGS coatings should be broader than those of the corresponding feedstock powder. However, in this case, the feedstock powder itself was extensively work-hardened; therefore, some recovery may have taken place during spraying. In the coatings, the diffraction signal from the undeformed particle cores thus reflected a partly recovered material, although the diffraction signal from the particle boundaries was affected by the plastic flow due to the adiabatic shear instability.

The lower amount of BCC phase might also have been a consequence of the annealing of the particles, either by the hot gases or by the adiabatic shear instability phenomenon itself, although both processes had a very short duration.

On the other hand, the narrow XRD peaks of the annealed Cantor powder had broadened after CGS deposition (Fig. 2A) and the amount of BCC phase increased again, due to the structural disorder introduced into the recrystallized feedstock powder by the solid-state impact. The peaks of the σ-phase were no longer visible in the XRD patterns of the Cantor coatings. It is unlikely that the σ-phase disappeared during the CGS deposition. Because of the broadening of the diffraction peaks, it is more likely that their intensity, which was already quite low in the pattern of the powder, decreased further and dropped below the background level.

4.2. Mechanical properties

All the microstructural differences between the HVOF and the CGS coatings had a measurable effect on their micromechanical properties, as revealed by the Vickers micro-indentation, depth-sensing spherical multi-cycle indentation, and nanoindentation maps.

For instance, the Vickers microhardness of the HVOF HEA coatings and their hardness and elastic modulus values from spherical indentation were slightly lower than those for the corresponding CGS samples. Some of the interlamellar oxide inclusions that were in the HVOF HEA coatings probably failed during the indentation tests, leading to a decrease in the measured response of the HVOF-sprayed coatings in terms of hardness and modulus. The systematic difference between the microhardness measured by Vickers indentation at 3 N load and by spherical indentation, with a maximum load of 400 mN, was also indirect evidence of some defects and brittle phases in the coatings. The hardness of thermal spray coatings often shows a scaling behaviour in relation to their lamellar microstructure. As the load increases, a larger volume of material is probed, which increases the likelihood of finding weak points that can fail and give way to the indenter [78].

The fact that the HVOF-sprayed Stellite coating, which contained fewer oxide inclusions, had higher hardness and elastic modulus also suggests that the oxide inclusions were the main source of brittleness in the HVOF-sprayed HEA coatings. The nanoindentation maps provided more conclusive evidence of this. As shown in the Supplementary

Material (Figure S15) and noted in Section 3.4.2, sometimes the nanoindentations made on the oxide inclusions of the HVOF coatings returned no usable load-penetration curve, almost as if the indenter had encountered a pore. This means that some of the oxide areas were brittle and defective, and collapsed under the action of the indenter.

Other inclusions, however, returned particularly high hardness values in the nanoindentation maps shown in the Supplementary Material (Figure S15), which means that in fact, many of the inclusions were very strong. This could explain the systematic difference that seemed to appear among the complete stress-strain curves (Section 3.4.1, Fig. 6) as a function of the oxide content of the coatings. In fact, the values of the work-hardening coefficient $b > 0.5$ in most of the HVOF-sprayed HEA coatings was unusually high for a metallic alloy of any kind. The large number of oxide inclusions in the HVOF-sprayed HEA coatings, many of which were very strong, probably offered multiple obstacles to dislocation motion, thus promoting the rapid work-hardening of the material. In contrast, in the CGS samples and in the HVOF Stellite coating, the lower number of oxide inclusions resulted in a more conventional behaviour: most of the work-hardening coefficients were in the range $0.2 < b < 0.3$ (Table 8).

While depth-sensing spherical indentation provided information on the overall mechanical behaviour of the coatings, nanoindentation maps provided more detailed information on the individual properties of different microstructural constituents, as already seen for the oxide inclusions.

As shown in Section 3.4.2, the Gaussian Mixture Model deconvolution enables us to identify sub-distributions within the complete nanoindentation datasets for each tested sample. The results (Table 9) showed that, sometimes, for a given sample, the number of data points within each of the elastic modulus sub-distributions differed from the number of data points in the corresponding sub-distributions of indentation hardness. In these cases, the sub-distributions in the indentation hardness and the elastic modulus data probably did not reflect the same "mechanical phases". This occurred because the volume of material affected by elastic deformation is always larger than the volume affected by plastic deformation. Therefore, despite being obtained from the same indentation experiment, the indentation hardness data had a better spatial resolution than the elastic modulus data and more reliably reflected the properties of actual phases in the material. For example, in the case of the HVOF Cantor Run2 sample, it is likely that the two sub-distributions fitted to the elastic modulus data, whose average values, as observed in Section 3.4.2, differed by less than the associated standard deviations, did not truly reflect two distinct phases.

The poorer spatial resolution and the fact that, perhaps, distinct phases (e.g. the FCC metal matrix and the oxide inclusions) had similar elastic moduli meant that there was probably only one distribution of the elastic modulus data. The elastic moduli in Table 9 were also only marginally higher than those obtained by spherical indentation (Fig. 5B, D, F, H, J), despite the higher load values employed in the latter experiments. This confirms that the elastic modulus values were more sensitive to the overall properties of the coating and less suited to the deconvolution of the properties of individual phases at the micro-scale.

The discussion hereafter thus focuses primarily on the indentation hardness distributions. In the case of the HVOF Cantor Run2 sample, for instance, two clearly distinguishable hardness distributions were evident. The main distribution, with an average close to 8.5 GPa, comprised most of the data; whereas a secondary distribution with a higher average of almost 12 GPa comprised only 17 % of the data. The latter probably corresponded to the hardness of the spinel-type oxide inclusions previously described. The oxides made up a larger volume fraction of the sample (Table 7), but as noted, some of the oxide regions were too defective to return a measurable value. The secondary distribution thus revealed the hardness of the oxide inclusions that were dense and free of defects. The main distribution, on the other hand, corresponded to the hardness of the FCC metallic phase. The average value of 8.5 GPa was much higher than the typical hardness of the bulk Cantor alloy [79]. The fine grain size and the intra-lamellar oxide inclusions, which were too small to be spatially resolvable from the surrounding metal, probably explain this very high hardness. The measured value thus reflected the hardness of an oxide-dispersion strengthened material.

In the HVOF-sprayed Al_0(CrMnFeNi), Al_{10}(CrMnFeNi), and Al_{14}(CrMnFeNi) coatings, three sub-distributions were identified (Table 9). The sub-distribution with the lowest average indentation hardness value, which was in the range of 5.5–6.5 GPa in all cases, corresponded to a decreasing fraction in the overall data as the content of Al in the alloy increased. In contrast, the number of values comprised in the sub-distribution with an intermediate $H_{IT} \sim 7 - 8$ GPa increased with the Al content. It is inferable that the first distribution corresponded to the softer FCC phase and the second distribution corresponded to the harder BCC phase, whose amounts varied inversely with increasing Al content (Section 3.2 and Table 6). The third distribution, characterized by the highest hardness values of $\sim 9.5 - 10.5$ GPa, could again correspond to the fraction of oxide inclusions that were free of defects and could generate usable load-penetration curves. The fraction of data points in the third distribution decreased with increasing Al content, which is consistent with the decrease in the volume fraction of oxides.

In the CGS Cantor Run1 sample, almost all the hardness data fell within a single distribution with a similar average value to the HVOF coating, i.e. $H_{IT} \sim 8$ GPa. This could again be regarded as the hardness of the FCC matrix with a dispersion of fine oxide inclusions. A small fraction of hardness values were comprised of a separate sub-distribution, characterized by an average value $H_{IT} \sim 9$ GPa, They could be due to the small fraction of BCC phase in the CGS Cantor coatings (Section 3.2, Fig. 2, and Table 6), to the σ-phase carried over from the feedstock powder (although this could not be detected by XRD as discussed previously), or to some of the biggest oxide particles. Another distribution with $H_{IT} \sim 6$ GPa could be attributed to indentations falling next to defects, such as some weak interparticle boundaries where the adiabatic shear instability-driven bonding could have been less effective. The presence of such poorly bonded areas is in fact shown in the Supplementary Material (Figure S8B). Similar considerations hold for the CGS Al_0(CrMnFeNi) coating, where three distributions with average hardness values of 6.8, 8.8, and 9.3 GPa were identified (Table 9), corresponding to indentations near a defect, in the main FCC phase, and in the secondary BCC phase, respectively.

4.3. Tribological behaviour under sliding wear conditions

The tribological behaviour of the coatings in the dry sliding wear tests also reflected the differences discussed so far. In particular, among the HVOF-sprayed coatings, the specific wear rate increased from the Cantor to the Al_0(CrMnFeNi), Al_{10}(CrMnFeNi), and Al_{14}(CrMnFeNi) coatings (Fig. 8A). This suggests that the wear loss increased with an increasing amount of BCC phase and a decreasing number of oxide inclusions. The CGS Cantor coatings, which wore a bit more than the HVOF-sprayed ones, also contained much fewer oxides and slightly more of the BCC phase. Sliding wear resistance appeared to have little relation with the overall microhardness of the coatings measured by the Vickers and depth-sensing spherical indentations. For example, the CGS Cantor coatings were harder than the HVOF-sprayed ones, but they exhibited a higher specific wear rate. Similarly, the HVOF-sprayed Al_{14}(CrMnFeNi) coatings were harder than the Al_0(CrMnFeNi) and Al_{10}(CrMnFeNi) ones but wore down more. The HVOF-sprayed Stellite coating also had a similar hardness to the CGS samples, but its wear rate was much lower.

The physical bases for these behaviours can be understood through the wear mechanisms. The worn surface of the HVOF Cantor coatings (Fig. 9A, B) indicated a combination of adhesive wear (ductile tearing) and tribo-oxidation (widespread formation of tribo-oxidized clusters), similar to the findings by Patel et al. [76]. The cross-sectional view in

Fig. 11A, B confirmed that an irregular layer of tribo-oxidized debris was compacted on the surface of the HVOF Cantor coatings. Adhesive wear, reflected by the plastic extrusion of metal (Fig. 11B – label 1), occurred where the metal surface was exposed. The cross-section also highlighted another important feature. Many of the oxide inclusions contained within the HVOF coating emerged on the outer surface (Fig. 11A, B: label 2) and bore part of the contact with the counterpart. Some of these inclusions were brittle, as discussed in Section 4.2, and, in fact, they sometimes tended to crack, as seen, for example, in the area labelled "2" in Fig. 11A. However, other inclusions were hard and strong enough to bear the contact pressure without cracking (e.g. the area labelled "2" in Fig. 11B). These stronger inclusions not only limited the contact pressure suffered by the metal phase, but they also interrupted the continuity of the metal phase itself. They thus limited the size of the metal fragments that could be torn out at once by a single event of adhesive tearing.

On the surfaces of the coatings that suffered higher wear rates, including the HVOF Al_{10}(CrMnFeNi) (Fig. 9C, D) and Al_{14}(CrMnFeNi) coatings (Fig. 9E, F) and the CGS coatings (Fig. 12A, B and C, D), the more extensive plastic flow indicated a more severe form of adhesive wear, whereas signs of tribo-oxidation were almost absent. Fig. 9D (label "1"), for example, shows a portion of the worn surface of a HVOF-sprayed Al_{10}(CrMnFeNi) sample where most of the material was ductile-fractured, consistent with a severe form of adhesive wear. Fig. 9F (label "3"), and Fig. 12B and D (label "1"), show many lips of material that were being plastically sheared out of the worn surfaces of the corresponding samples.

Figure S18 in the Supplementary Material shows that the mass fraction of oxygen detected by EDX analyses at various locations along the worn surface was much higher in the HVOF Cantor coatings. In the Al_x(CrMnFeNi) coatings, the oxygen content on the worn surface decreased continuously, except for a few specific locations that corresponded to irregularly distributed oxide clusters. This corroborated the decreasing incidence of tribo-oxidation in samples that exhibited increasingly high specific wear rates.

An increasingly large fraction of the counterpart surface (Fig. 10B-F) was also covered with shiny patches of transferred metal as the wear loss of the corresponding coating increased. For example, after sliding against an HVOF Al_{14}(CrMnFeNi) coating, the surface of the ball was almost entirely covered by large lips of metal that were reminiscent of those seen on the worn surface of the coating in Fig. 9F, thus confirming that severe adhesive transfer was occurring.

Correspondingly, on the polished cross-section of the HVOF Al_{14}(CrMnFeNi) coating, the re-transferring of plastically deformed debris and the ductile shearing of the metal described in Section 3.5.2 were typical signs of adhesive wear [80].

These observations thus corroborate the assumption that the oxide inclusions, at least those that did not tend to break up under load, restrained the adhesive tearing of the metal. On a more stable surface that wore down at a lower rate, the accumulation of clusters of tribo-oxidized debris then became possible, which further limited the extension of exposed metal and helped limit the wear loss.

In principle, the HVOF Al_{10}(CrMnFeNi) and Al_{14}(CrMnFeNi) coatings should have benefitted from the higher hardness of the BCC phase in their metal matrix (see the previous discussion on the hardness of individual phases in Section 4.2). In fact, the authors in [81–85] reported that the addition of Al increased the wear resistance of transition metal-based HEAs, both in the form of sintered bulk and as laser-cladded and HVOF-sprayed coatings. The main reason was reportedly the higher hardness, associated both with solid-solution strengthening and the transition from an FCC-based to a BCC-based system.

Why this did not happen in the present case could be explained by the TEM analysis of the near-surface regions of the worn samples. The ~1 μm thick layer of fine-grained material next to the worn surface of the HVOF Al_{14}(CrMnFeNi) Run3 coating was indicative of dynamic recrystallization. This can, in fact, occur when a metal is subjected to high levels of plastic strain, such as those induced by adhesion to and dragging by the counterpart during the ball-on-disc tests. Under these conditions, the numerous dislocations generated in the material tended to arrange into low-angle boundaries which then evolved into high-angle boundaries between newly formed nanometric grains. The dynamic recrystallization in the Al_{14}(CrMnFeNi) coatings is consistent with Stachowiak and Batchelor [86] who found that dynamic recovery was easier for materials with higher stacking fault energy (SFE) [86]. In fact, according to the literature, adding Al to transition metals-based HEAs increases their SFE [87,88] and hinders the occurrence of twinning [89]. Adhesive tearing and delamination primarily affected this recrystallized layer, as testified by the delamination crack and the tearing event shown in Fig. 13A and described in Section 3.5.2 [90,91]. The multi-cycle spherical indentation tests suggested that all the HVOF coatings should have been capable of significant work-hardening when plastically strained (Section 4.2), which should have restrained the occurrence of adhesive wear. However dynamic recrystallization countered this tendency to work-harden and, thus, worsened the wear resistance, as also suggested by Stachowiak and Batchelor [86]. The contradiction between the results of indentation and sliding wear was probably due to the different stress conditions in the two tests. The repeated action of large shear stresses during the sliding wear test, and the correspondingly large shear strains, were absent in the spherical indentation test. The shear strain component might have played a key role in inducing dynamic recrystallization.

In addition, the SAED analyses indicated that the dynamic recrystallization favoured the formation of an FCC structure. It was not possible to run nanoindentation experiments directly on the recrystallized layer, due to its very small size, however, as noted above, the nanoindentation results on as-deposited coatings (Table 9) indicated that the FCC phase was softer than the BCC phase. There was thus no benefit from the harder BCC phase in the metal matrix of the HVOF Al_{14}(CrMnFeNi) coating because dynamic recrystallization led to the formation of a pure FCC layer on the surface.

The same TEM analysis on the HVOF-sprayed Cantor Run2 coating revealed that the recrystallized layer was much thinner (Fig. 14, Section 3.5.2). Again, this can be ascribed to the oxide inclusions, which bore part of the contact with the counterpart and interrupted the continuity of the metal phase, thus limiting the extent to which the metal was plastically dragged. A similar finding has also been reported in bulk HEAs. Reviewing recent findings, Kumar [19] reported that a spark plasma sintered HEA obtained from a mechanically alloyed powder, which consisted of a fine-grained FCC structure with dispersed hard phases (oxides and μ-phase) had good sliding wear resistance. This material developed a near-surface tribolayer where the hard phases prevented excessive plastic flow of the ductile FCC matrix.

In the HVOF-sprayed Cantor coating, the thin recrystallized layer was not associated with any phase change, since the same FCC structure existed in the recrystallized layer and in the interior of the coating.

It follows that the currently chosen HEA compositions could not be hardened by a stress-induced phase change mechanism: the Cantor composition did not exhibit phase change, while the Al_{14}(CrMnFeNi) developed a softer FCC phase. This behaviour probably decisively contributed to the poorer wear resistance of the present samples in comparison with the Stellite reference. Stellite alloys are known to undergo a stress-induced martensitic phase change from an FCC to an HCP lattice, which is associated with substantial hardening [41,92]. Our previous research on HVOF-sprayed Stellite coatings also confirmed this phenomenon. FIB+TEM analysis showed that a micrometre-thick surface layer of stress-induced HCP phase was developed during ball-on-disc testing [49].

In fact, the HVOF Stellite coating tested in this work did not show signs of severe adhesive tearing (Fig. 12F), which was prevented by the high hardness of the HCP "martensite" layer formed during the test. Therefore, wear proceeded through the slow delamination of the HCP layer by surface fatigue (micropitting – label "2" in Fig. 12F) and

through abrasion caused by the hard asperities on the counterpart and the debris trapped in the contact region.

The same mechanisms probably explain the difference between the trends in the friction curves of the HEA coatings and the HVOF Stellite coating, as mentioned in Section 3.5.1. They probably also caused the corresponding difference in the trends in specific wear rates with increasing sliding distance. The transition from a lower- to a higher-friction regime in the HVOF Stellite coating, and the decrease in the specific wear rate from 1000 m to 5000 m, could have been associated with the complete development of the hard "martensitic" surface layer. This layer slowed down the wear loss but increased the abrasive component of friction because more energy was needed to plough and cut through the harder surface. In the early stages, by contrast, greater wear and lower friction might have occurred due to the greater ease of ploughing through a softer surface. The same transition from a lower to a higher friction stage after a sliding distance of around 500 m was also observed in our previous experiments with HVOF-sprayed Stellite [49]. This therefore seems to be a repeatable behaviour for this type of coating. Conversely, in the HVOF Cantor Run1 coating, which attained a steady friction regime very early and did not exhibit any stress-induced phase change, the specific wear rate did not change when the sliding distance was increased from 1000 m to 5000 m.

It could be concluded from the present results that designing and choosing HEA compositions capable of stress-induced hardening, either through martensitic transformation or by transformation- and twinning-induced plasticity (TRIP, TWIP) mechanisms, could be the key to obtaining a sliding wear resistance that is comparable to or better than conventional alloys.

As a final note, the increasing incidence of adhesive wear resulted in a slight decrease, instead of an increase, in the friction coefficient recorded during the sliding wear tests. In fact, the HVOF-sprayed Cantor coatings produced higher friction coefficients than the Al_{10}(CrMnFeNi) and Al_{14}(CrMnFeNi) samples, and the HVOF-sprayed Stellite coating produced the highest friction coefficients of all the tests (Fig. 8C). In this case, the wear track itself, with its periodically varying width (Fig. 12E), suggested a stick-slip phenomenon.

It is possible that the oxidized clusters formed on the surface of the HVOF-sprayed Cantor coating, while effective against wear, did not reduce the tangential force needed to maintain relative motion. Other researchers have already reported that non-crystalline tribo-oxides (in terms of the tribo-oxidation of WC-Co based coatings [93,94]) tend to develop high friction. Another factor might be the hygroscopicity of these fine, oxidized debris particles. When oxide clusters formed on the two mating surfaces, high shear stresses might therefore have been needed to break the strong bond between them. In the case of the Stellite coating, the very hard surface layer formed by the "martensitic" transformation could have also increased the energy expenditure needed for the counterpart to continue ploughing through the coating, as noted previously.

4.4. Electrochemical corrosion behaviour

The results showed that the corrosion resistance of the HEA coatings worsened with the increasing content of Al. This is consistent with findings reported in the literature for bulk HEAs [22–24,95,96]: the corrosion current density increased with the addition of Al, and the passivation ability became substantially worse. According to the literature, this was probably due to the formation of a 2-phase microstructure, with BCC and FCC phases, which resulted in galvanic coupling and a worsening of the stability of the passive film.

The corrosion current density values (Fig. 16), especially for the HVOF HEA coatings, were of the same order of magnitude as those reported in the literature for bulk transition metal-based HEAs with and without Al, which are in the range of 10^{-8} to 10^{-7} A/cm^2 when tested in aqueous NaCl solutions [23,96,97]. Other thermally sprayed HEA coatings, such as the HVOF-sprayed equiatomic AlCrFeCoNi coating by Löbel et al. [98], also exhibited corrosion current density of the order of 10^{-7} A/cm^2 in an NaCl solution. However, compared to the corrosion behaviour of bulk HEAs, the diverse microstructures induced by the deposition processes had a substantial effect. Most notable was the poorer performance of the CGS samples compared to the corresponding HVOF-sprayed ones, despite the apparent density and much lower content of oxide inclusions of the CGS coatings. This behaviour, which was also found by Silvello et al. when comparing HVOF and CGS Cantor coatings [59], could be explained by analysing the cross-sections of the corroded samples.

In the HVOF coatings, the corrosive agents penetrated below the surface through the lamellar boundaries and attacked individual lamellae, leaving behind an almost empty "skeleton" consisting of oxide inclusions and a few residual metal strips.

The penetration might have been favoured by defects in the inter-lamellar oxide inclusions and/or at the interface between the oxides and the metal. Because some spinel-type oxides are electrically conductive, they might also have acted as cathodes, accelerating the anodic dissolution of the metal. Notably, a mostly metallic layer remained on the outer surface of the samples as observed in Fig. 17A-B, which suggested that the corrosion was much more severe immediately below the surface. The mechanism was probably akin to crevice corrosion. Since oxygen could not easily access the interior of the coating, the passivation of the material was hindered, promoting the dissolution of the metal just below the outer "skin". In the CGS coatings (Fig. 17C, D), the damage was at least as extensive, but in this case there was no recognizable outer skin. When viewed in detail (Fig. 17D), the corrosion damage followed the patterns of plastic deformation in the as-deposited material (see Fig. 4B for the same composition).

Mahaffey et al. [99] also found that the corrosion behaviour of a CGS HEA coating (specifically, a Cantor alloy coating) was primarily influenced by the retention of the microstructure of the feedstock powder. In that case, the feedstock powder was gas atomized, and its key feature was solute segregation in the interdendritic regions, which thus became the preferential sites for corrosion. In our CGS samples, by contrast, the main issue was the presence of plastically strained metal. With its higher content of lattice defects and its many interfaces and grain boundaries, plastically strained metal is more prone to corrosion. Thus, the conditions for accelerated corrosion damage of the present CGS coatings resulted from:

(1) The retention of the microstructure of the HEBM powders, which, especially in the case of the as-milled Al_0(CrMnFeNi) feedstock, consisted of welded sheets of plastically deformed metal.

(2) The additional plastic flow induced by the CGS process through the adiabatic shear instabilities.

The chemical inhomogeneities carried over from the feedstock powder to the CGS coatings, as discussed in Section 3.2, also worsened the corrosion resistance by providing many micro-galvanic couples. Future research could explore whether more extensive annealing of the feedstock powders and/or the CGS coatings themselves could improve the corrosion resistance by promoting full recrystallization and interdiffusion.

5. Conclusions

In this work, four high-entropy alloy (HEA) compositions, namely equiatomic Cr-Mn-Fe-Co-Ni ("Cantor" alloy) and $Al_x(Cr_{20}Mn_{25}Fe_{40}Ni_{15})_{100-x}$ with x = 0, 10 and 14, were synthesized by mechanical alloying through high-energy ball milling (HEBM) and deposited on AISI304 stainless steel plates by HVOF spraying and cold gas spraying (CGS). The results of a comprehensive set of microstructural, mechanical, sliding wear, and electrochemical corrosion tests led us to the following conclusions:

– The HEBM HEA powders were prone to oxidation during the HVOF spraying process, resulting in oxide contents that ranged from

maxima of ~40 vol% in Al-free compositions to ~20 vol% in Al-rich systems. The difference was due to the formation of dense Al oxides which limited the formation of spinel-type mixed oxides affecting the transition metal constituents. These oxide contents were much higher than those of a reference Stellite coating deposited by the same HVOF process using a commercially available (gas atomized) feedstock powder.

- The HVOF coatings did not retain the severely work-hardened microstructure of the feedstock powder. Most of the particles melted during spraying and then re-solidified upon impact or (sometimes) in flight, resulting in a combination of columnar grains, submicrometric equiaxed grains, and coarser (micrometric) equiaxed grains. The resulting phase composition of the HVOF coatings was similar to that expected at the solidus temperature of the corresponding alloys. However, some excess of the FCC phase was observed, which appeared in small amounts even in unexpected compositions, such as the $Al_{10}(Cr_{20}Mn_{25}Fe_{40}Ni_{15})_{90}$ and $Al_{14}(Cr_{20}Mn_{25}Fe_{40}Ni_{15})_{86}$ systems.
- CGS, on the other hand, caused much less additional oxidation, although the CGS coatings had a higher oxygen content than the feedstock powders. The CGS coatings mostly retained the original microstructure of the feedstock powders, which showed a dispersion of fine oxide particles and chemical inhomogeneities due to incomplete interdiffusion among the metallic constituents. Those inhomogeneities were, instead, eliminated by the HVOF spraying.
- The elastic moduli of the CGS coatings measured by spherical nanoindentation (~180 – 200 GPa) were slightly higher than those measured on the corresponding HVOF-sprayed coatings (~150 – 170 GPa). This was due to the good cohesion of the CGS samples and the brittleness of some of the oxide inclusions in the HVOF coatings, which failed inelastically during indentation.
- Nanoindentation mapping enabled the identification of the "intrinsic" hardness of the individual phases of the coatings. In materials with multi-phase metallic matrices, such as the $Al_{10}(Cr_{20}Mn_{25}Fe_{40}Ni_{15})_{90}$ and $Al_{14}(Cr_{20}Mn_{25}Fe_{40}Ni_{15})_{86}$ compositions, the BCC phase (H_{IT} ~ 8 – 9 GPa) was harder than the FCC phase (H_{IT} ~ 5 – 7 GPa), as expected, and both phases were much harder than in bulk HEAs. This was due to the fine grain structure, the oxide inclusions (in the HVOF coatings), and, in the CGS coatings, the work-hardening retained from the as-milled powder and/or induced by the deposition.
- The sliding wear rates of the coatings ranged from ~6×10^{-5} $mm^3/(N•m)$ for the HVOF-sprayed Cantor coatings to ~8×10^{-4} $mm^3/(N•m)$ for the HVOF-sprayed $Al_{14}(Cr_{20}Mn_{25}Fe_{40}Ni_{15})_{86}$ coatings. The sliding wear rate appeared to worsen with an increase in the amount of the BCC phase and a decrease in the number of oxide inclusions in the coatings. In fact, the oxide inclusions helped to limit the size of the metallic regions that were plastically sheared and torn from the worn surface by adhesion to the counterpart. They thus promoted a shift from adhesive to tribo-oxidative wear. Samples that were more severely worn were shown to develop a micrometre-thick recrystallized layer near the surface. Re-crystallization probably impaired the ability of the material to work-harden and, therefore, led to even more severe adhesive wear. The thick recrystallized layer of the HVOF $Al_{14}(Cr_{20}Mn_{25}Fe_{40}Ni_{15})_{86}$ coatings was also found to develop a softer FCC phase. No phase change instead occurred in the FCC Cantor coatings. Thus, none of the coatings exhibited any stress-induced surface hardening mechanism. This lack of any intrinsic hardening process could explain why the wear loss of the HEA coatings was higher than that of the HVOF-sprayed Stellite reference. in fact, Stellite is known for its martensitic transformation from an FCC structure to an HCP structure during wear.
- The HVOF-sprayed HEA coatings exhibited low corrosion current densities in the range of 0.4–1 μA/cm^2, which was lower than the HVOF-sprayed Stellite reference (~1.5 μA/cm^2), although they exhibited narrower pseudo-passivity ranges. The HVOF-sprayed Cantor coatings exhibited comparatively wider pseudo-passivity ranges and lower corrosion current densities, whereas the $Al_x(Cr_{20}Mn_{25}Fe_{40}Ni_{15})_{100-x}$ coatings had a narrower pseudo-passivity range. As the amount of Al increased, passivity became increasingly restricted (i.e. with a narrower pseudo-passivity range) until it disappeared completely, and the corrosion current density increased correspondingly.
- The CGS coatings had a worse corrosion resistance than the HVOF-sprayed ones because the corrosion damage was promoted by the plastically deformed microstructure that characterized these coatings. This effect was partially caused by the retention of the HEBM particles' microstructure and, in part, by the additional plastic deformation produced in the particles during the deposition.

CRediT authorship contribution statement

Edoardo Rossi: Writing – review & editing, Investigation, Formal analysis. **Luca Bortolotti:** Writing – review & editing, Investigation, Formal analysis. **Marco Sebastiani:** Writing – review & editing, Supervision, Investigation, Formal analysis. **Alessia Bruera:** Investigation. **Enrico Forlin:** Writing – review & editing, Methodology, Investigation, Conceptualization. **Giovanni Bolelli:** Writing – original draft, Visualization, Supervision, Project administration, Methodology, Investigation, Funding acquisition, Formal analysis, Data curation, Conceptualization. **Giulia Gigante:** Writing – review & editing, Investigation, Formal analysis. **Maria Francesca Bonilauri:** Writing – review & editing, Investigation, Formal analysis. **Alessandro Togni:** Investigation. **Alvise Bianchin:** Writing – review & editing, Supervision, Project administration, Methodology, Investigation, Funding acquisition, Conceptualization. **Felice Palladino:** Investigation. **Sergi Dosta:** Writing – review & editing, Supervision, Investigation, Formal analysis. **Luca Lusvarghi:** Writing – review & editing, Supervision, Funding acquisition, Conceptualization. **Stefania Morelli:** Writing – review & editing, Investigation, Formal analysis. **Genís Clavé:** Writing – review & editing, Investigation, Formal analysis. **Lorenzo Ferrari:** Investigation, Formal analysis. **Camila Barreneche:** Writing – review & editing, Investigation, Formal analysis. **Magdalena Lassinantti Gualtieri:** Writing – review & editing, Investigation, Formal analysis.

Declaration of Competing Interest

The authors declare the following financial interests/personal relationships which may be considered as potential competing interests. All authors report financial support was provided by European Union. Alvise Bianchin, Enrico Forlin report a relationship with MBN Nanomaterialia s.r.l. that includes: employment. If there are other authors, they declare that they have no known competing financial interests or personal relationships that could have appeared to influence the work reported in this paper.

Acknowledgements

This work was funded by the European Union under the GA no 101092211; Project name: "Integrated Computational-Experimental material Engineering of Thermal Spray coatings"; Project acronym: "CoBRAIN"; call topic: HORIZON-CL4-2022-RESILIENCE-01-19; Granting authority: European Health and Digital Executive Agency (HADEA). However the views and opinions expressed are those of the author(s) only and do not necessarily reflect those of the European Union or HADEA and thus neither the European Union nor the granting authority can be held responsible for them.

The authors would like to thank Dr. Miriam Hanuskova (University of Modena and Reggio Emilia, Modena, Italy) for performing the particle size distribution analyses on the feedstock powders.

The authors are also grateful to the company partner Titomic Europe B.V. (Akkrum, NL) for spraying the cold gas spray samples.

Appendix A. Supporting information

Supplementary data associated with this article can be found in the online version at doi:10.1016/j.jallcom.2025.183050.

References

[1] B. Cantor, Multicomponent high-entropy cantor alloys, Prog. Mater. Sci. 120 (2021) 100754, https://doi.org/10.1016/j.pmatsci.2020.100754.
[2] B. Cantor, Multicomponent and high entropy alloys, Entropy 16 (2014) 4749–4768, https://doi.org/10.3390/e16094749.
[3] S.S. Nene, S. Sinha, D.K. Yadav, A. Dutta, Metallurgical aspects of high entropy alloys, J. Alloy. Compd. 1005 (2024) 175849, https://doi.org/10.1016/J.JALLCOM.2024.175849.
[4] X. Chang, M. Zeng, K. Liu, L. Fu, Phase engineering of High-Entropy alloys, Adv. Mater. 32 (2020), https://doi.org/10.1002/adma.201907226.
[5] E. Olorundaisi, P.A. Olubambi, The prospect and limitation of high entropy alloy as 4th industrial material, Mater. Today Sustain. 31 (2025) 101163, https://doi.org/10.1016/J.MTSUST.2025.101163.
[6] Z. Li, S. Zhao, R.O. Ritchie, M.A. Meyers, Mechanical properties of high-entropy alloys with emphasis on face-centered cubic alloys, Prog. Mater. Sci. 102 (2019) 296–345, https://doi.org/10.1016/j.pmatsci.2018.12.003.
[7] D.B. Miracle, O.N. Senkov, A critical review of high entropy alloys and related concepts, Acta Mater. 122 (2017) 448–511, https://doi.org/10.1016/j.actamat.2016.08.081.
[8] F. Yu, B. Yang, A. Liu, E. Zhu, W. Zhang, Machine learning-driven design of high-entropy alloys: phase prediction, performance optimization, and challenges, J. Alloy. Compd. 1036 (2025) 181898, https://doi.org/10.1016/J.JALLCOM.2025.181898.
[9] O.N. Senkov, J.D. Miller, D.B. Miracle, C. Woodward, Accelerated exploration of multi-principal element alloys for structural applications, CALPHAD 50 (2015) 32–48, https://doi.org/10.1016/j.calphad.2015.04.009.
[10] F. Tancret, I. Toda-Caraballo, E. Menou, P.E.J. Rivera Díaz-Del-Castillo, Designing high entropy alloys employing thermodynamics and Gaussian process statistical analysis, Mater. Des. 115 (2017) 486–497, https://doi.org/10.1016/j.matdes.2016.11.049.
[11] S. Guo, C. Ng, J. Lu, C.T. Liu, Effect of valence electron concentration on stability of fcc or bcc phase in high entropy alloys, J. Appl. Phys. 109 (2011) 103505, https://doi.org/10.1063/1.3587228.
[12] Y. Zhang, T.T. Zuo, Z. Tang, M.C. Gao, K.A. Dahmen, P.K. Liaw, Z.P. Lu, Microstructures and properties of high-entropy alloys, Prog. Mater. Sci. 61 (2014) 1–93, https://doi.org/10.1016/j.pmatsci.2013.10.001.
[13] S.A. Krishna, N. Noble, N. Radhika, B. Saleh, A comprehensive review on advances in high entropy alloys: fabrication and surface modification methods, properties, applications, and future prospects, J. Manuf. Process 109 (2024) 583–606, https://doi.org/10.1016/j.jmapro.2023.12.039.
[14] F. Zhang, Y. Wu, H. Lou, Z. Zeng, V.B. Prakapenka, E. Greenberg, Y. Ren, J. Yan, J. S. Okasinski, X. Liu, Y. Liu, Q. Zeng, Z. Lu, Polymorphism in a high-entropy alloy, Nat. Commun. 8 (2017) 15687, https://doi.org/10.1038/ncomms15687.
[15] R.K. Nutor, Q. Cao, X. Wang, S. Ding, D. Zhang, J.-Z. Jiang, Accelerated emergence of CoNi-based medium-entropy alloys with emphasis on their mechanical properties, Curr. Opin. Solid State Mater. Sci. 26 (2022) 101032, https://doi.org/10.1016/j.cossms.2022.101032.
[16] F.G. Coury, G. Zepon, C. Bolfarini, Multi-principal element alloys from the CrCoNi family: outlook and perspectives, J. Mater. Res. Technol. 15 (2021) 3461–3480, https://doi.org/10.1016/j.jmrt.2021.09.095.
[17] S. Ragunath, N. Radhika, B. Saleh, Advancements and future prospects of additive manufacturing in high-entropy alloy applications, J. Alloy. Compd. 997 (2024) 174859, https://doi.org/10.1016/j.jallcom.2024.174859.
[18] M.Y. Abdul Salam, E.N. Ogunmuyiwa, V.K. Manisa, A. Yahya, I.A. Badruddin, Effect of fabrication techniques of high entropy alloys: a review with integration of machine learning, Results Eng. 25 (2025) 104441, https://doi.org/10.1016/j.rineng.2025.104441.
[19] D. Kumar, Recent advances in tribology of high entropy alloys: a critical review, Prog. Mater. Sci. 136 (2023) 101106, https://doi.org/10.1016/J.PMATSCI.2023.101106.
[20] J. Dąbrowa, M. Danielewski, State-of-the-Art diffusion studies in the high entropy alloys, Met. (Basel) 10 (2020) 347, https://doi.org/10.3390/met10030347.
[21] B. Gludovatz, A. Hohenwarter, D. Catoor, E.H. Chang, E.P. George, R.O. Ritchie, A fracture-resistant high-entropy alloy for cryogenic applications, Science 345 (1979) (2014) 1153–1158, https://doi.org/10.1126/science.1254581.
[22] Y. Fu, J. Li, H. Luo, C. Du, X. Li, Recent advances on environmental corrosion behavior and mechanism of high-entropy alloys, J. Mater. Sci. Technol. 80 (2021) 217–233, https://doi.org/10.1016/J.JMST.2020.11.044.
[23] Y. Qiu, S. Thomas, M.A. Gibson, H.L. Fraser, N. Birbilis, Corrosion of high entropy alloys, Npj Mater. Degrad. 1 (2017) 15, https://doi.org/10.1038/s41529-017-0009-y.
[24] J.Y. Zhang, B. Xiao, T.H. Chou, B.X. Cao, Y.L. Zhao, B. Liu, K. Huang, S.B. Yang, J. C. Su, Y. Liu, T. Yang, High-Entropy alloys: a critical review of aqueous corrosion behavior and mechanisms, High. Entropy Alloy. Mater. 1 (2023) 195–259, https://doi.org/10.1007/s44210-023-00021-z.
[25] J. Wu, Y. Chen, H. Zhu, A review on the tribological performances of High-Entropy alloys, Adv. Eng. Mater. 24 (2022), https://doi.org/10.1002/adem.202101548.
[26] J. Zhou, J. Yang, X. Zhang, F. Ma, K. Ma, Y. Cheng, Research status of tribological properties optimization of high-entropy alloys: a review, J. Mater. Sci. 58 (2023) 4257–4291, https://doi.org/10.1007/s10853-023-08255-3.
[27] J. Liang, W. Wang, Z. Cao, J. Guo, Z. Sun, Y. Hai, Corrosion resistance and mechanism of high-entropy alloys: a review, Mater. Corros. 75 (2024) 424–432, https://doi.org/10.1002/maco.202313975.
[28] M. Ghorbani, Z. Li, Y. Qiu, P. Marcus, J.R. Scully, O. Gharbi, H. Luo, R.K. Gupta, Z. R. Zeng, H.L. Fraser, M.L. Taheri, N. Birbilis, Current progress in aqueous corrosion of Multi-Principal element alloys, Metall. Mater. Trans. A 55 (2024) 2571–2588, https://doi.org/10.1007/s11661-024-07473-x.
[29] M. Cagirici, S. Guo, J. Ding, U. Ramamurty, P. Wang, Additive manufacturing of high-entropy alloys: current status and challenges, Smart Mater. Manuf. 2 (2024) 100058, https://doi.org/10.1016/j.smmf.2024.100058.
[30] B. Chen, Progress in additive manufacturing of High-Entropy alloys, Materials 17 (2024) 5917, https://doi.org/10.3390/ma17235917.
[31] Y. Liu, D. Xiang, K. Wang, T. Yu, Corrosion of laser cladding High-Entropy alloy coatings: a review, Coatings 12 (2022) 1669, https://doi.org/10.3390/coatings12111669.
[32] N. Gong, T.L. Meng, J. Cao, Y. Wang, R. Karyappa, C.K. Ivan Tan, A. Suwardi, Q. Zhu, A.C.Y. Ngo, K.P. Misra, R.D.K. Misra, H. Liu, Laser-cladding of high entropy alloy coatings: an overview, Mater. Technol. 38 (2023), https://doi.org/10.1080/10667857.2022.2151696.
[33] H. Xie, Y. Tong, Y. Bai, X. Li, Y. Han, K. Hua, H. Wang, Wear-Resistance of High-Entropy alloy coatings and High-Entropy Alloy-Based composite coatings prepared by the laser cladding technology: a review, Adv. Eng. Mater. 25 (2023), https://doi.org/10.1002/adem.202300426.
[34] Z.U. Arif, M.Y. Khalid, E. ur Rehman, S. Ullah, M. Atif, A. Tariq, A review on laser cladding of high-entropy alloys, their recent trends and potential applications, J. Manuf. Process 68 (2021) 225–273, https://doi.org/10.1016/j.jmapro.2021.06.041.
[35] P. Zhang, Z. Li, H. Liu, Y. Zhang, H. Li, C. Shi, P. Liu, D. Yan, Recent progress on the microstructure and properties of high entropy alloy coatings prepared by laser processing technology: a review, J. Manuf. Process 76 (2022) 397–411, https://doi.org/10.1016/j.jmapro.2022.02.006.
[36] C. Lin, Y. Yao, Corrosion-Resistant coating based on High-Entropy alloys, Met. (Basel) 13 (2023) 205, https://doi.org/10.3390/met13020205.
[37] R. Bhaskaran Nair, R. Supekar, S. Morteza Javid, W. Wang, Y. Zou, A. McDonald, J. Mostaghimi, P. Stoyanov, High-Entropy alloy coatings deposited by thermal spraying: a review of strengthening mechanisms, performance assessments and perspectives on future applications, Met. (Basel) 13 (2023) 579, https://doi.org/10.3390/met13030579.
[38] D. Luo, Q. Zhou, Z. Huang, Y. Li, Y. Liu, Q. Li, Y. He, H. Wang, Tribological behavior of high entropy alloy coatings: a review, Coatings 12 (2022) 1428, https://doi.org/10.3390/coatings12101428.
[39] Z.U. Arif, M.Y. Khalid, A. Al Rashid, E. ur Rehman, M. Atif, Laser deposition of high-entropy alloys: a comprehensive review, Opt. Laser Technol. 145 (2022) 107447, https://doi.org/10.1016/j.optlastec.2021.107447.
[40] K. Lu, J. Zhu, D. Guo, M. Yang, H. Sun, Z. Wang, X. Hui, Y. Wu, Microstructures, corrosion resistance and wear resistance of High-Entropy alloys coatings with various compositions prepared by laser cladding: a review, Coatings 12 (2022) 1023, https://doi.org/10.3390/coatings12071023.
[41] D.H.E. Persson, On the mechanisms behind the tribological performance of stellites, Uppsala University, 2005. ⟨http://www.diva-portal.org/smash/get/diva2:167455/FULLTEXT01.pdf⟩.
[42] X.Z. Zhang, R. Liu, K.Y. Chen, M.X. Yao, R. Collier, Electrochemical study of corrosion behavior of wrought stellite alloys in sodium chloride and Green death solutions, J. Mater. Eng. Perform. 24 (2015) 3579–3587, https://doi.org/10.1007/s11665-015-1629-4.
[43] N. Cinca, E. López, S. Dosta, J.M. Guilemany, Study of stellite-6 deposition by cold gas spraying, Surf. Coat. Technol. 232 (2013) 891–898, https://doi.org/10.1016/j.surfcoat.2013.06.120.
[44] C. N, G. JM, Cold gas sprayed Stellite-6 coatings and their wear resistance, J. Mater. Sci. Eng. 02 (2013) 1000122, https://doi.org/10.4172/2169-0022.1000122.
[45] H.S. Sidhu, B.S. Sidhu, S. Prakash, Solid particle erosion of HVOF sprayed NiCr and Stellite-6 coatings, Surf. Coat. Technol. 202 (2007) 232–238, https://doi.org/10.1016/j.surfcoat.2007.05.035.
[46] C. Navas, A. Conde, M. Cadenas, J. De Damborenea, Tribological properties of laser clad stellite 6 coatings on steel substrates, Surf. Eng. 22 (2006) 26–34, https://doi.org/10.1179/174329406x84949.
[47] S.-S. Chang, H.-C. Wu, C. Chen, Impact wear resistance of stellite 6 hardfaced valve seats with laser cladding, Mater. Manuf. Process. 23 (2008) 708–713, https://doi.org/10.1080/10426910802317102.
[48] Š. Houdková, Z. Pala, E. Smazalová, M. Vostřák, Z. Česánek, Microstructure and sliding wear properties of HVOF sprayed, laser remelted and laser clad stellite 6 coatings, Surf. Coat. Technol. 318 (2017) 129–141, https://doi.org/10.1016/j.surfcoat.2016.09.012.
[49] P. Sassatelli, G. Bolelli, M. Lassinantti Gualtieri, E. Heinonen, M. Honkanen, L. Lusvarghi, T. Manfredini, R. Rigon, M. Vippola, Properties of HVOF-sprayed Stellite-6 coatings, Surf. Coat. Technol. 338 (2018) 45–62, https://doi.org/10.1016/j.surfcoat.2018.01.078.
[50] R.A. Seraj, A. Abdollah-zadeh, S. Dosta, H. Assadi, I.G. Cano, Comparison of stellite coatings on low carbon steel produced by CGS and HVOF spraying, Surf. Coat. Technol. 372 (2019) 299–311, https://doi.org/10.1016/J.SURFCOAT.2019.05.022.

[51] D. Lison, M. De Boeck, V. Verougstraete, M. Kirsch-Volders, Update on the genotoxicity and carcinogenicity of cobalt compounds, Occup. Environ. Med 58 (2001) 619–625, https://doi.org/10.1136/oem.58.10.619.
[52] D. Lison, S. van den Brule, G. Van Maele-Fabry, Cobalt and its compounds: update on genotoxic and carcinogenic activities, Crit. Rev. Toxicol. 48 (2018) 522–539, https://doi.org/10.1080/10408444.2018.1491023.
[53] M. Suh, C.M. Thompson, G.P. Brorby, L. Mittal, D.M. Proctor, Inhalation cancer risk assessment of cobalt metal, Regul. Toxicol. Pharmacol. 79 (2016) 74–82, https://doi.org/10.1016/j.yrtph.2016.05.009.
[54] CLH report: Proposal for Harmonised Classification and Labelling Based on Regulation (EC) No 1272/2008 (CLP Regulation), Annex VI, Part 2. Substance Name: Cobalt, (2019) 1–157. ⟨https://echa.europa.eu/documents/10162/d1ca0305-88d5-5b07-69ee-1f4312c1951f⟩ (accessed March 22, 2019).
[55] Commission Delegated Regulation (EU) 2020/217 of 4 October 2019 amending, for the purposes of its adaptation to technical and scientific progress, Regulation (EC) No 1272/2008 of the European Parliament and of the Council on classification, labelling and packaging of substances and mixtures and correcting that Regulation, 2020. ⟨https://eur-lex.europa.eu/eli/reg_del/2020/217/oj/eng⟩ (accessed January 16, 2025).
[56] C.E.L. Latunussa, K. Georgitzikis, C.T. de Matos, M. Grohol, U. Eynard, D. Wittmer, L. Mancini, M. Unguru, C. Pavel, S. Carrara, F. Mathieux, D. Pennington, G.A. Blengini, Study on the EU's list of Critical Raw Materials (2020), Factsheets on Critical Raw Materials, Luxembourg, 2020. https://doi.org/10.2873/92480.
[57] G.A. Blengini, C. EL Latunussa, U. Eynard, C. Torres de Matos, D. Wittmer, K. Georgitzikis, C. Pavel, S. Carrara, L. Mancini, M. Unguru, D. Blagoeva, F. Mathieux, D. Pennington, Study on the EU's list of Critical Raw Materials – Final Report, Brussels, Belgium, 2020. https://doi.org/10.2873/11619.
[58] M. Kumaravel, S. Bagherifard, M. Guagliano, Advancements in deposition of high entropy alloys using cold spray technology, J. Therm. Spray. Technol. 34 (2025) 1–36, https://doi.org/10.1007/S11666-024-01879-0.
[59] A. Silvello, P. Cavaliere, S. Yin, R. Lupoi, I. Garcia Cano, S. Dosta, Microstructural, mechanical and wear behavior of HVOF and Cold-Sprayed High-Entropy alloys (HEAs) coatings, J. Therm. Spray. Technol. 31 (2022) 1184–1206, https://doi.org/10.1007/s11666-021-01293-w.
[60] N.D. Stepanov, D.G. Shaysultanov, R.S. Chernichenko, M.A. Tikhonovsky, S. V. Zherebtsov, Effect of al on structure and mechanical properties of Fe-Mn-Cr-Ni-Al non-equiatomic high entropy alloys with high fe content, J. Alloy. Compd. 770 (2019) 194–203, https://doi.org/10.1016/j.jallcom.2018.08.093.
[61] G. Bolelli, A. Colella, L. Lusvarghi, S. Morelli, P. Puddu, E. Righetti, P. Sassatelli, V. Testa, TiC–NiCr thermal spray coatings as an alternative to WC-CoCr and Cr_3C_2–NiCr, Wear 450451 (2020) 203273, https://doi.org/10.1016/j.wear.2020.203273.
[62] R. Pero, N. Randall, D. Frey, R.N. Widmer, T. Darby, L. Aucott, C. Hardie, S. Pak, P. Maquet, A. Bushby, Stress-strain curve mapping by nanoindentation – a technique to qualify diffusion-bonded window assemblies for ITER, Fusion Eng. Des. 196 (2023) 113977, https://doi.org/10.1016/j.fusengdes.2023.113977.
[63] A. Bhat, R.W. Neu, On the constraint factor relating uniaxial and indentation yield strength of polycrystalline materials using spherical microindentation, Mater. Perform. Charact. 9 (2020) 324–345, https://doi.org/10.1520/MPC20190260.
[64] W.C. Oliver, G.M. Pharr, An improved technique for determining hardness and elastic modulus using load and displacement sensing indentation experiments, J. Mater. Res 7 (1992) 1564–1583, https://doi.org/10.1557/JMR.1992.1564.
[65] E. Rossi, J.M. Wheeler, M. Sebastiani, High-speed nanoindentation mapping: a review of recent advances and applications, Curr. Opin. Solid State Mater. Sci. 27 (2023) 101107, https://doi.org/10.1016/j.cossms.2023.101107.
[66] P. Sudharshan Phani, W.C. Oliver, A critical assessment of the effect of indentation spacing on the measurement of hardness and modulus using instrumented indentation testing, Mater. Des. 164 (2019) 107563, https://doi.org/10.1016/j.matdes.2018.107563.
[67] H. Besharatloo, J.M. Wheeler, Influence of indentation size and spacing on statistical phase analysis via high-speed nanoindentation mapping of metal alloys, J. Mater. Res 36 (2021) 2198–2212, https://doi.org/10.1557/s43578-021-00214-5.
[68] D. Tabor, The hardness of metals, Oxford University Press, Oxford, UK, 2000, https://doi.org/10.1093/oso/9780198507765.001.0001.
[69] G. Bolelli, M.F. Bonilauri, L. Bortolotti, A. Bruera, M. Cescon, L. Ferrari, M. L. Gualtieri, L. Lusvarghi, S. Morelli, M. Pazzi, A. Bianchin, E. Forlin, G. Gigante, E. Rossi, M. Sebastiani, HVOF deposition of TiC-based hardmetal coatings with High-Entropy alloy (HEA) matrix, Surf. Coat. Technol. Submitt. (2025) 132386, https://doi.org/10.1016/j.surfcoat.2025.132386.
[70] E. Colombini, M. Lassinantti Gualtieri, C. Mortalò, S.M. Deambrosis, P. Veronesi, In-house synthesis of CoCrFeNi ingots using an electric furnace, Mater. Lett. 323 (2022) 132571, https://doi.org/10.1016/J.MATLET.2022.132571.
[71] J. Wang, T. Guo, J. Li, W. Jia, H. Kou, Microstructure and mechanical properties of non-equilibrium solidified CoCrFeNi high entropy alloy, Mater. Chem. Phys. 210 (2018) 192–196, https://doi.org/10.1016/J.MATCHEMPHYS.2017.06.037.
[72] S. Sampath, H. Herman, Rapid solidification and microstructure development during plasma spray deposition, J. Therm. Spray. Technol. 5 (1996) 445–456, https://doi.org/10.1007/BF02645275.
[73] S. Deshpande, S. Sampath, H. Zhang, Mechanisms of oxidation and its role in microstructural evolution of metallic thermal spray coatings - case study for Ni-Al, Surf. Coat. Technol. 200 (2006) 5395–5406, https://doi.org/10.1016/j.surfcoat.2005.07.072.
[74] S. Kamnis, A.K. Sfikas, B. Allcock, S. Gonzalez, HVOF processed CoCrFeMnNi High-entropy alloy coatings: a combined computational and experimental validation approach, J. Therm. Spray. Technol. 31 (2022) 1000–1010, https://doi.org/10.1007/S11666-021-01268-X.
[75] M. Löbel, T. Lindner, M. Grimm, L.-M. Rymer, T. Lampke, Influence of aluminum and molybdenum on the microstructure and corrosion behavior of thermally sprayed High-Entropy alloy coatings, J. Therm. Spray. Technol. 31 (2022) 1366–1374, https://doi.org/10.1007/s11666-021-01297-6.
[76] P. Patel, S.A. Alidokht, N. Sharifi, A. Roy, K. Harrington, P. Stoyanov, R. R. Chromik, C. Moreau, Microstructural and tribological behavior of thermal spray CrMnFeCoNi high entropy alloy coatings, J. Therm. Spray. Technol. 31 (2022) 1285–1301, https://doi.org/10.1007/s11666-022-01350-y.
[77] H. Assadi, F. Gärtner, T. Stoltenhoff, H. Kreye, Bonding mechanism in cold gas spraying, Acta Mater. 51 (2003) 4379–4394, https://doi.org/10.1016/S1359-6454(03)00274-X.
[78] J. Nohava, B. Bonferroni, G. Bolelli, L. Lusvarghi, Interesting aspects of indentation and scratch methods for characterization of thermally-sprayed coatings, Surf. Coat. Technol. 205 (2010) 1127–1131, https://doi.org/10.1016/j.surfcoat.2010.08.086.
[79] S. Gorsse, M.H. Nguyen, O.N. Senkov, D.B. Miracle, Database on the mechanical properties of high entropy alloys and complex concentrated alloys, Data Brief. 21 (2018) 2664–2678, https://doi.org/10.1016/j.dib.2018.11.111.
[80] G.W. Stachowiak, A.W. Batchelor, Adhesion and adhesive wear. in: Engineering Tribology, Elsevier, Oxford, UK, 2014, pp. 577–596, https://doi.org/10.1016/B978-0-12-397047-3.00012-6.
[81] S. Sabarinath, V. Raj, L.V. Nair, V. Thomas, N. Ogunlakin, V.S. Saji, High entropy alloy (HEA) coatings for tribological applications - a review, Results Eng. 27 (2025) 105695, https://doi.org/10.1016/J.RINENG.2025.105695.
[82] F. Zhang, X. Chen, H. Liu, L. Che, L. Pan, T. Zhou, C. Guo, Recent developments in CoCrFeNi-based high entropy alloy coatings: design, synthesis, and properties, J. Alloy. Compd. 1018 (2025) 179193, https://doi.org/10.1016/J.JALLCOM.2025.179193.
[83] S. Li, Y. Sun, Z. Liu, L. Zhou, T. Wu, Y. Bai, Evolution of tribological properties of laser cladding 3D transition metal high entropy alloy coatings, J. Mater. Sci. 2025 60:9 (60) (2025) 4118–4147, https://doi.org/10.1007/S10853-025-10695-Y.
[84] T. Zirari, V. Trabadelo, A review on wear, corrosion, and wear-corrosion synergy of high entropy alloys, Heliyon 10 (2024), https://doi.org/10.1016/J.HELIYON.2024.E25867.
[85] R. Bhaskaran Nair, R. Supekar, S. Morteza Javid, W. Wang, Y. Zou, A. McDonald, J. Mostaghimi, P. Stoyanov, High-Entropy alloy coatings deposited by thermal spraying: a review of strengthening mechanisms, performance assessments and perspectives on future applications, Met. (Basel) 13 (2023) 579, https://doi.org/10.3390/met13030579.
[86] G.W. Stachowiak, A.W. Batchelor, Abrasive, erosive and cavitation wear, in: Engineering Tribology, Elsevier B.V., Amsterdam, NL, 2014, pp. 525–576, https://doi.org/10.1016/S0167-8922(08)70585-6.
[87] X. Zhang, R. Dong, Q. Guo, H. Hou, Y. Zhao, Predicting the stacking fault energy in FCC high-entropy alloys based on data-driven machine learning, J. Mater. Res. Technol. 26 (2023) 4813–4824, https://doi.org/10.1016/J.JMRT.2023.08.194.
[88] X. Sun, H. Zhang, W. Li, X. Ding, Y. Wang, L. Vitos, Generalized stacking fault energy of Al-Doped CrMnFeCoNi High-Entropy alloy, Nanomaterials 10 (2019) 59, https://doi.org/10.3390/nano10010059.
[89] S. Qiu, X.C. Zhang, J. Zhou, S. Cao, H. Yu, Q.M. Hu, Z. Sun, Influence of lattice distortion on stacking fault energies of CoCrFeNi and Al-CoCrFeNi high entropy alloys, J. Alloy. Compd. 846 (2020) 156321, https://doi.org/10.1016/J.JALLCOM.2020.156321.
[90] H. Al-Maliki, D. Künstner, S. Scheriau, K. Six, G. Trummer, Methodology to assess damage mechanisms of rail steels based on small-scale experiments, Wear 530531 (2023) 205052, https://doi.org/10.1016/J.WEAR.2023.205052.
[91] G. Trummer, C. Marte, P. Dietmaier, C. Sommitsch, K. Six, Modeling surface rolling contact fatigue crack initiation taking severe plastic shear deformation into account, Wear 352353 (2016) 136–145, https://doi.org/10.1016/J.WEAR.2016.02.008.
[92] D.H.E. Persson, S. Jacobson, S. Hogmark, Antigalling and low friction properties of a laser processed Co-based material, J. Laser Appl. 15 (2003) 115–119, https://doi.org/10.2351/1.1514218.
[93] J.A.R. Wesmann, N. Espallargas, Effect of atmosphere, temperature and carbide size on the sliding friction of self-mated HVOF WC-CoCr contacts, Tribol. Int 101 (2016) 301–313, https://doi.org/10.1016/j.triboint.2016.04.032.
[94] J.A.R. Wesmann, S. Kuroda, N. Espallargas, The role of oxide tribofilms on friction and wear of different thermally sprayed WC-CoCr, J. Therm. Spray. Technol. 26 (2017) 492–502, https://doi.org/10.1007/s11666-017-0522-0.
[95] Y. Shi, B. Yang, X. Xie, J. Brechtl, K.A. Dahmen, P.K. Liaw, Corrosion of AlxCoCrFeNi high-entropy alloys: Al-content and potential scan-rate dependent pitting behavior, Corros. Sci. 119 (2017) 33–45, https://doi.org/10.1016/j.corsci.2017.02.019.
[96] M. Izadi, M. Soltanieh, S. Alamolhoda, S.M.S. Aghamiri, M. Mehdizade, Microstructural characterization and corrosion behavior of AlxCoCrFeNi high entropy alloys, Mater. Chem. Phys. 273 (2021), https://doi.org/10.1016/j.matchemphys.2021.124937.
[97] Y. Qiu, S. Thomas, D. Fabijanic, A.J. Barlow, H.L. Fraser, N. Birbilis, Microstructural evolution, electrochemical and corrosion properties of

AlxCoCrFeNiTiy high entropy alloys, Mater. Des. 170 (2019) 107698, https://doi.org/10.1016/j.matdes.2019.107698.

[98] M. Löbel, T. Lindner, T. Mehner, L.-M. Rymer, S. Björklund, S. Joshi, T. Lampke, Microstructure and corrosion properties of AlCrFeCoNi High-Entropy alloy coatings prepared by HVAF and HVOF, J. Therm. Spray. Technol. 31 (2022) 247–255, https://doi.org/10.1007/s11666-021-01255-2.

[99] J. Mahaffey, A. Vackel, S. Whetten, M. Melia, A.B. Kustas, Structure evolution and corrosion performance of CoCrFeMnNi high entropy alloy coatings produced via plasma spray and cold spray, J. Therm. Spray. Technol. 31 (2022) 1143–1154, https://doi.org/10.1007/s11666-022-01373-5.